The Wavy Ekman Layer: Langmuir Circulations, Breaking Waves, and Reynolds Stress

JAMES C. MCWILLIAMS, EDWARD HUCKLE, AND JUN-HONG LIANG

IGPP, University of California, Los Angeles, Los Angeles, California

PETER P. SULLIVAN

MMM, NCAR, Boulder, Colorado

(Manuscript received 10 January 2012, in final form 8 May 2012)

ABSTRACT

Large-eddy simulations are made for the canonical Ekman layer problem of a steady wind above a uniformly rotating, constant-density ocean. The focus is on the influence of surface gravity waves: namely, the wave-averaged Stokes-Coriolis and Stokes-vortex forces and parameterized wave breaking for momentum and energy injection. The wave effects are substantial: the boundary layer is deeper, the turbulence is stronger, and eddy momentum flux is dominated by breakers and Langmuir circulations with a vertical structure inconsistent with both the conventional logarithmic layer and eddy viscosity relations. The surface particle mean drift is dominated by Stokes velocity with Langmuir circulations playing a minor role. Implications are assessed for parameterization of the mean velocity profile in the Ekman layer with wave effects by exploring several parameterization ideas. The authors find that the *K*-profile parameterization (KPP) eddy viscosity is skillful for the interior of the Ekman layer with wave-enhanced magnitude and depth scales. Furthermore, this parameterization form is also apt in the breaker and Stokes layers near the surface when it is expressed as a Lagrangian eddy viscosity (i.e., turbulent Reynolds stress proportional to vertical shear of the Lagrangian mean flow, inclusive of Stokes drift) with a derived eddy-viscosity shape and with a diagnosed vertical profile of a misalignment angle between Reynolds stress and Lagrangian mean shear.

1. Introduction

The Ekman layer is the quintessential oceanic surface turbulent boundary layer. Its canonical formulation is a steady surface wind stress, $\tau = \rho_o u_*^2$ (u_* the oceanic ''friction velocity''), on top of an ocean with uniform density ρ_o and uniform rotation rate f (Coriolis frequency) aligned with the vertical direction. The analytic steady solution with constant eddy viscosity κ_o has a surface current to the right of the stress direction (with $f > 0$) and a further rightward spiral decay over a depth interval $\sim\sqrt{\kappa_o/f}$. With a turbulent boundary layer parameterization, for example, *K*-profile parameterization (KPP) (Large et al. 1994; McWilliams and Huckle 2006), $\kappa(z)$ has a convex shape and a magnitude $\sim u_*^2/f$—hence, a depth scale $\sim u_*/f$. Large-eddy simulation (LES)—with an explicit calculation of the turbulent eddies, their Reynolds stress, and the mean current—provides a validation standard for parameterizations to be used in large-scale circulation models (Zikanov et al. 2003).

The same winds that cause the Ekman layer also cause surface gravity waves, either in local equilibrium with the wind or in disequilibrium due to a transient history or remote propagation. The combination of wind and waves has a significant impact on the (wavy) Ekman layer, most importantly through the generation of turbulent Langmuir circulations (LCs) and modification of the Coriolis force through the wave-averaged Stokes drift profile $u_{st}(z)$ acting as ''vortex forces'' (Skyllingstad and Denbo 1995; McWilliams et al. 1997; plus many subsequent studies reviewed in Sullivan and McWilliams 2010). Furthermore, especially for high winds and waves, the momentum transmission from atmospheric winds to oceanic currents by surface drag occurs primarily through isolated impulses associated with wind-generated surface waves when they break and penetrate into the ocean, rather than through a uniform τ at the surface; this is represented in a stochastic breaker model (Sullivan et al. 2007).

Corresponding author address: James C. McWilliams, IGPP, University of California, Los Angeles, Los Angeles, CA 90095-1567. E-mail: jcm@atmos.ucla.edu

DOI: 10.1175/JPO-D-12-07.1

This paper reports on LES solutions of the Ekman layer problem, which is a simpler boundary layer configuration than most prior studies that include a depth-limiting stable density stratification and surface buoyancy flux.[1] We contrast the Ekman layer without wave effects to the wavy layer with both Stokes drift and breaker impulse forcing, in various combinations to distinguish particular influences. The primary focus is on how the coherent structures, LCs, and breaker-induced circulations relate to the turbulent Reynolds stress—hence, the mean current profile—to be able to assess the requirements for a successful parameterization of the wavy Ekman layer. Because we do not include buoyancy effects, nonstationarity, or other types of currents nor do we survey a variety of different wave wind regimes, our results only provide an idealized case study rather than a more comprehensive characterization of wave effects in the surface boundary layer. Nevertheless, for this case it demonstrates their importance and salient characteristics.

2. Problem setup

The LES code solves the wave-averaged dynamical equations in Sullivan and McWilliams (2010) with forcing options among a uniform mean surface stress τ^x, fields of stochastic breaker acceleration $A(\mathbf{x}, t)$ and subgrid-scale energy injection rate $W(\mathbf{x}, t)$ or mean breaker vertical profiles, $\langle A\rangle(z)$ and $\langle W\rangle(z)$. (Mean refers to time and horizontal averages, denoted by angle brackets; z is the vertical coordinate.) The forcing options are normalized to give the same mean vertically integrated force; that is, $\int \langle A\rangle\, dz = \tau^x/\rho_o = u_*^2$. The LES model includes a subgrid-scale parameterization scheme that generalizes the turbulent kinetic energy balance and eddy viscosity model in Moeng (1984) with the additional Stokes drift and breaker work effects in Sullivan and McWilliams (2010).

We focus on a particular situation where the forcing is aligned with $\hat{\mathbf{x}}$ (east), and the wind speed at 10-m height is $U_a = 15$ m s^{-1} [implying a surface stress of 0.35 N m^{-2}; hence, velocity $u_* = (|\tau^x|/\rho_o)^{1/2} = 1.9 \times 10^{-2}$ m s^{-1}]. The wave elevation spectrum [determining the Stokes drift profile $u_{\rm st}(z)$] and breaker spectrum (determining A and W) are empirically consistent with equilibrium for this wind for a wave age of $c_p/u_{*a} = 19$ (c_p is the phase speed of the wave elevation spectrum peak and $u_{*a} = \sqrt{\rho_o/\rho_a}\,u_*$ is the atmospheric friction velocity).[2] The profiles of $\langle A\rangle(z)$ and $u_{\rm st}(z)$ are shown in Fig. 1. Both are surface intensified and have characteristic vertical length scales (defined, somewhat arbitrarily, as the depth where the amplitude has decreased to 10% of its surface value) of $h_b = 1.4$ m and $h_{\rm st} = 13$ m, respectively. Both of these are much smaller than the turbulent boundary layer depth h_o; the ordering $h_b \ll h_{\rm st} \ll h_o$ is typical in the ocean. For full wave elevation and breaker spectra, as used here, there is no uniquely correct vertical scale definition, and we use these estimates only as a rough guide for the vertical profiles shown below. We will see that the flow structure and dynamical balances are distinctive in three sublayers within the overall Ekman layer, which we designate as the breaker, Stokes, and interior shear layers. We choose a midlatitude Coriolis frequency, $f = 10^{-4}$ s^{-1}: hence, an Ekman boundary layer dimensional depth scale of $u_*/f = 190$ m. The domain size is $L_x \times L_y \times L_z = 500$ m $\times$ 500 m $\times$ 300 m, large enough to encompass the Ekman layer and its energetic turbulent eddies. The horizontal grid cell size is $dx = dy = 1.7$ m, and the vertical grid is nonuniform in the vertical with a minimum cell size $dz = 0.42$ m near the surface and maximum of $dz = 5$ m at the bottom where the flow is nearly quiescent. Solutions are spun up from rest to a statistical equilibrium state after about one inertial period, $2\pi/f$. The solution analyses are made over a subsequent interval of several inertial periods, with temporally filtering to exclude the inertial oscillation in the horizontally averaged current at each vertical level. All our analysis results are presented in nondimensional form using appropriate factors of u_* and f.

In this paper we distinguish among different wave effects by defining six different cases, all of which have the same mean momentum forcing (i.e., the same u_*). The case without any wave effects is designated as $N\tau$, where N denotes the exclusion of Stokes drift influences and τ denotes a surface-stress boundary condition; this is the classical Ekman problem. The case with fullest wave effects is SB, where S denotes the inclusion of Stokes drift and B denotes stochastic breaker forcing; we view

[1] Polton et al. (2005) and Polton and Belcher (2007) also analyze simulations of an unstratified Ekman layer with Stokes drift.

[2] This age is somewhat young compared to full wind–wave equilibrium, with $c_p/u_{*a} = 30$. Younger waves have relatively fewer, larger breakers, and we make this choice to allow better resolution for a given spatial grid. Our conclusion in section 5 is that the details of the A and W profiles are only important within the breaker layer, so the age choice is not determinative overall. See Sullivan et al. (2007) for details about how the elevation and breaker spectra are specified from measurements and related to $u_{\rm st}$, A, and W consistent with conservation of momentum and energy in the air–wave–water system.

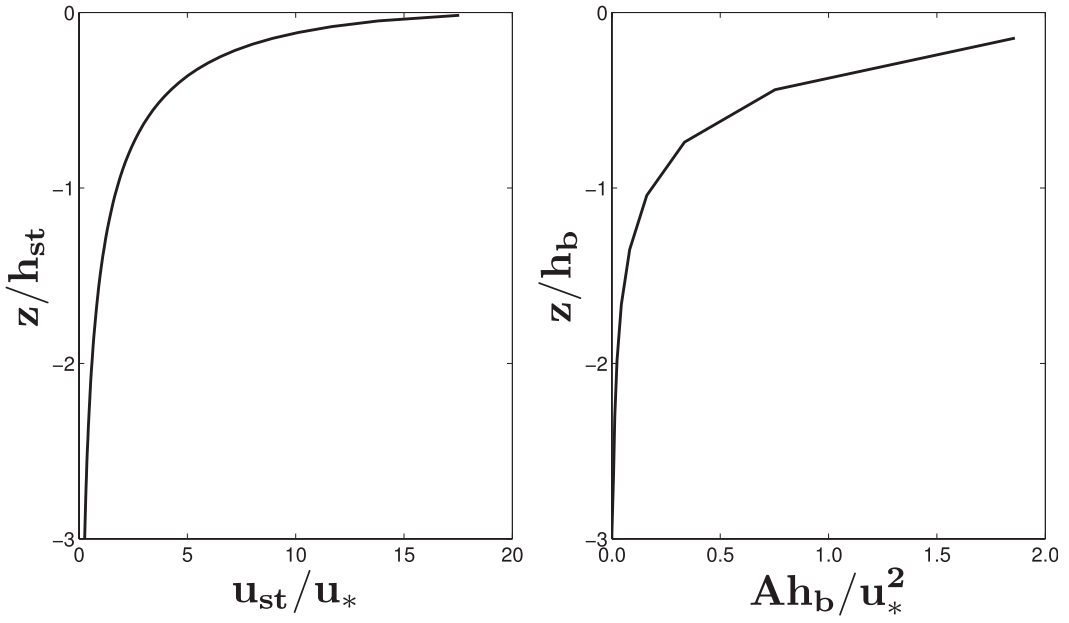

FIG. 1. Normalized profiles of (left) Stokes velocity $u_{st}(z)$ and (right) mean breaker acceleration $\langle A\rangle(z)$. The dimensional length scales are $h_{st} = 13.2$ m and $h_b = 1.4$ m, each defined as the depth at which the profile is 10% of its maximum at the shallowest grid level in the model.

this case as the most complete representation of wave effects. Intermediate partial wave-effect cases are $S\tau$ and NB. In addition, to understand the importance of the transient breaker forcing, we define cases $N\langle B\rangle$ and $S\langle B\rangle$ in which the four-dimensional (4D) fields of acceleration and energy-injection rate are replaced by their 1D mean profiles: $\langle A\rangle(z)$ and $\langle W\rangle(z)$.

3. Solution analysis

a. Bulk statistics

Table 1 gives several bulk statistics for the six cases. These include the mean boundary layer depth h_o; the depth-integrated value of the turbulent kinetic energy[3] profile,

$$e(z) = 0.5\langle \mathbf{u}'^2\rangle + \langle e^s\rangle \tag{1}$$

[i.e., the sum of the large-eddy velocity-fluctuation energy and the local subgrid-scale kinetic energy density e^s as parameterized in LES; the superscript prime denotes a fluctuation about the horizontal average and the superscript s refers to a $(\mathbf{x}, t)$ local variable in the subgrid-scale energy model]; and the total depth-integrated energy injection rate,[4] $\int \mathcal{E}^{\text{tot}}\, dz$, associated with either surface stress, $\tau^x\langle u\rangle(0)/\rho_o$, or breaker forcing, $\int \langle Au + W\rangle\, dz$. The velocity component u is the x velocity in the direction of the wind and waves, and v, w are the transverse and vertical velocities in the y, z directions. All quantities in the table are listed nondimensionally.

We immediately see several important wave effects. Stokes drift and vortex forces make the turbulent Ekman layer about twice as deep, independent of how the momentum forcing occurs. This effect would be much smaller in the more commonly analyzed situation with a stable pycnocline limiting the boundary layer depth. Vortex forces also increase the kinetic energy, $\int e\, dz$, again by about a factor of 2. The injection rate $\int \mathcal{E}^{\text{tot}}\, dz$ is largest with breaker forcing, mainly because W is large, and this enhancement has a similar magnitude with either stochastic or mean breaker forcing and with either u_{st} present or not; the injection rate is slightly smaller in $\langle B\rangle$ cases than B cases because the fluctuation

[3] This is distinct from the mean kinetic energy profile, $\bar{e}(z) = 0.5\langle \mathbf{u}_\perp\rangle^2$. See section 3c and appendix A.

[4] $\int \mathcal{E}^{\text{tot}}\, dz$ is the breaker and stress injection for the combined mean and turbulent energies, $e^{\text{tot}} = \bar{e} + e$. It is the sum of the work associated with the mean flow, $\int \bar{\mathcal{E}}\, dz = \tau^x\langle u\rangle(0)/\rho_o + \int \langle A\rangle\langle u\rangle\, dz$, plus the integral of $\mathcal{E}$ defined in (8) associated with breaker fluctuations A' and subgrid-scale energy injection W. This separation is relevant to the separate mean $\bar{e}$ and turbulent e balances. See section 3c and appendix A for the full energy balances.

TABLE 1. The six cases used in this study. The depth h_o is defined as the depth at which the magnitude of the turbulent stress is 10% of its surface value. The third column is the total kinetic energy per unit area. The fourth and fifth columns are the total energy input rate $\int \mathcal{E}^{\text{tot}}\, dz$ for τ and B cases, respectively.

Case	$h_o f/u_*$	$\int e\, dz\, f u_*^{-3}$	$\rho_o^{-1}\tau^x \langle u\rangle(0) u_*^{-3}$	$\int \langle Au + W\rangle\, dz\, u_*^{-3}$
$N\tau$	0.46	0.98	14	
$N\langle B\rangle$	0.45	1.24		242
NB	0.46	1.14		265
$S\tau$	1.06	2.26	0.8	
$S\langle B\rangle$	1.06	2.49		234
SB	0.94	2.10		261

correlation effect, $\langle A'u'\rangle$, is absent. There is also a noticeable difference in $\mathcal{E}^{\text{tot}}$ between the stress forcing cases with and without Stokes drift (i.e., $S\tau$ and $N\tau$, respectively); we will see in section 3b that the $S\tau$ case injection rate is smaller than the $N\tau$ case because $\langle u\rangle(0)$ is much reduced through the effect of the Stokes–Coriolis vortex force.[5] The enhanced boundary layer depth is consistent with the idea that, when Stokes drift is important, the relevant turbulent velocity scale is a composite one,

$$u_{*\text{com}} = u_*^{2/3} u_{\text{st}\,o}^{1/3}. \tag{2}$$

This scale is derived by assuming that Stokes–Reynolds stress production in the turbulent kinetic energy (TKE) balance (i.e., $\mathcal{P}_{\text{st}} \sim u_*^2 u_{\text{st}}/h_{\text{st}}$ in section 3c) enters into a dominant balance with dissipation rate $\epsilon \sim u_{*\text{com}}^3/h_{\text{st}}$. Because $u_{\text{st}}(z)$ is more than 10 times larger than u_* near the surface[6] (Fig. 1), the estimate $u_{*\text{com}}/f$ for h_o is more than twice as deep with Stokes drift, consistent with Table 1. The relevance of $u_{*\text{com}}$ to the TKE balance has been previously validated in stratification-limited Ekman layers (Harcourt and D'Asaro 2008; Grant and Belcher 2009; Kukulka et al. 2010) where h_o does not satisfy the Ekman scaling relation.[7] Also, $\int e$ increases by about a factor of 2 with u_{st} present, but this does not scale well with a bulk estimate using the composite velocity scale, $u_{*\text{com}}^3/f$ (10 times larger). The enhanced $\mathcal{E}^{\text{tot}}$ is consistent with the idea of breaker injection of TKE and a local production–dissipation TKE balance (Craig and Banner 1994), and it is also consistent with measurements of enhanced ϵ near the surface (Terray et al. 1996). Remarkably, there is not a direct relation between $\mathcal{E}^{\text{tot}}$ and the turbulent energy $\int e\, dz$ itself. Breaker forcing strongly enhances energy input, hence dissipation, yet it does not increase e greatly. Nor does $\mathcal{E}^{\text{tot}}$ increase only because u_{st} is present, as would be suggested by the increase in $u_{*\text{com}}$ (cf. cases $N\tau$ and $S\tau$). This demonstrates a degree of decoupling between e itself and the energy cycle throughput rates, $\mathcal{E}^{\text{tot}}$ and ϵ, so that the conventional turbulent scaling of $\epsilon \sim e^{3/2}/h$, for some turbulent length scale h, does not hold across the various combinations with u_{st} and B. Furthermore, because eddy viscosity is commonly estimated as $\kappa \sim e^{1/2}h$, this result also raises a question about how to express the idea that breaker energy injection leads to enhanced turbulent mixing near the surface. The increase of e with u_{st} does support the idea of enhanced mixing by the LCs sustained by the vortex force; however, the increase in $\int e\, dz$ is not by as much as a simple scaling estimate $\sim u_{*\text{com}}^3/f$, and the diagnosed value of κ (section 3d) increases by far more than $e^{1/2}h$ does. In summary, Stokes drift effects increase the boundary layer depth and turbulent energy, and breakers increase the energy cycle rate, but these enhancements are not collectively well represented by simple bulk scaling estimates, even with the composite velocity scale $u_{*\text{com}}$ in (2).

b. Mean velocity and momentum balance

The mean momentum balance is

$$\begin{aligned} 0 &= f\langle v\rangle - \partial_z\langle uw\rangle + \langle A\rangle \\ 0 &= -f(\langle u\rangle + u_{st}) - \partial_z\langle vw\rangle, \end{aligned} \tag{3}$$

with an associated surface condition of $\langle \mathbf{u}_\perp w\rangle = -\rho_o^{-1}\tau^x \hat{\mathbf{x}}$ at $z = 0$ (i.e., it is zero in the B cases). These balances contain the mean Coriolis and Stokes-Coriolis force, the mean breaker acceleration $\langle A\rangle$, and the divergence of the total horizontal turbulent Reynolds stress,

$$\langle \mathbf{u}_\perp w\rangle = \langle \mathbf{u}'_\perp w'\rangle + \langle \tau^s_{\perp z}\rangle. \tag{4}$$

τ^s_{ij} is the local subgrid-scale stress tensor as evaluated in the LES parameterization model. The index notation is i and j for all three spatial directions, $\perp$ for a horizontal vector component, and z for a vertical

[5] In case $S\tau$ the small wind stress injection is not the dominant energy source, which rather are Stokes-Coriolis and Stokes production conversions with the surface waves (section 3c and appendix A).

[6] For a full wave spectrum, the choice of $u_{\text{st}\,o}$ is somewhat delicate because $u_{\text{st}}(z)$ near the surface is sensitive to the spectrum shape. So, we prefer to view this scaling estimate for $u_{*\text{com}}$ qualitatively rather than precisely. Similarly, the turbulent Langmuir number, $La_t = \sqrt{u_{\text{st}\,o}/u_*}$, is an useful indicator of the wind wave dynamical regime (McWilliams et al. 1997), but it too depends on $u_{\text{st}\,o}$. From Fig. 1 we see that La_t is a bit smaller than 0.3 in our S cases, close to a local wind wave equilibrium value.

[7] Harcourt and D'Asaro (2008) propose a modified form of $u_{*\text{com}}$ with different vertical weighting of $u_{\text{st}}(z)$ for use in scaling the variance of w under more general circumstances. Kukulka et al. (2010) propose another modification when $\langle u\rangle(0)/u_{\text{st}\,o}$ is not small (unlike in our S cases).

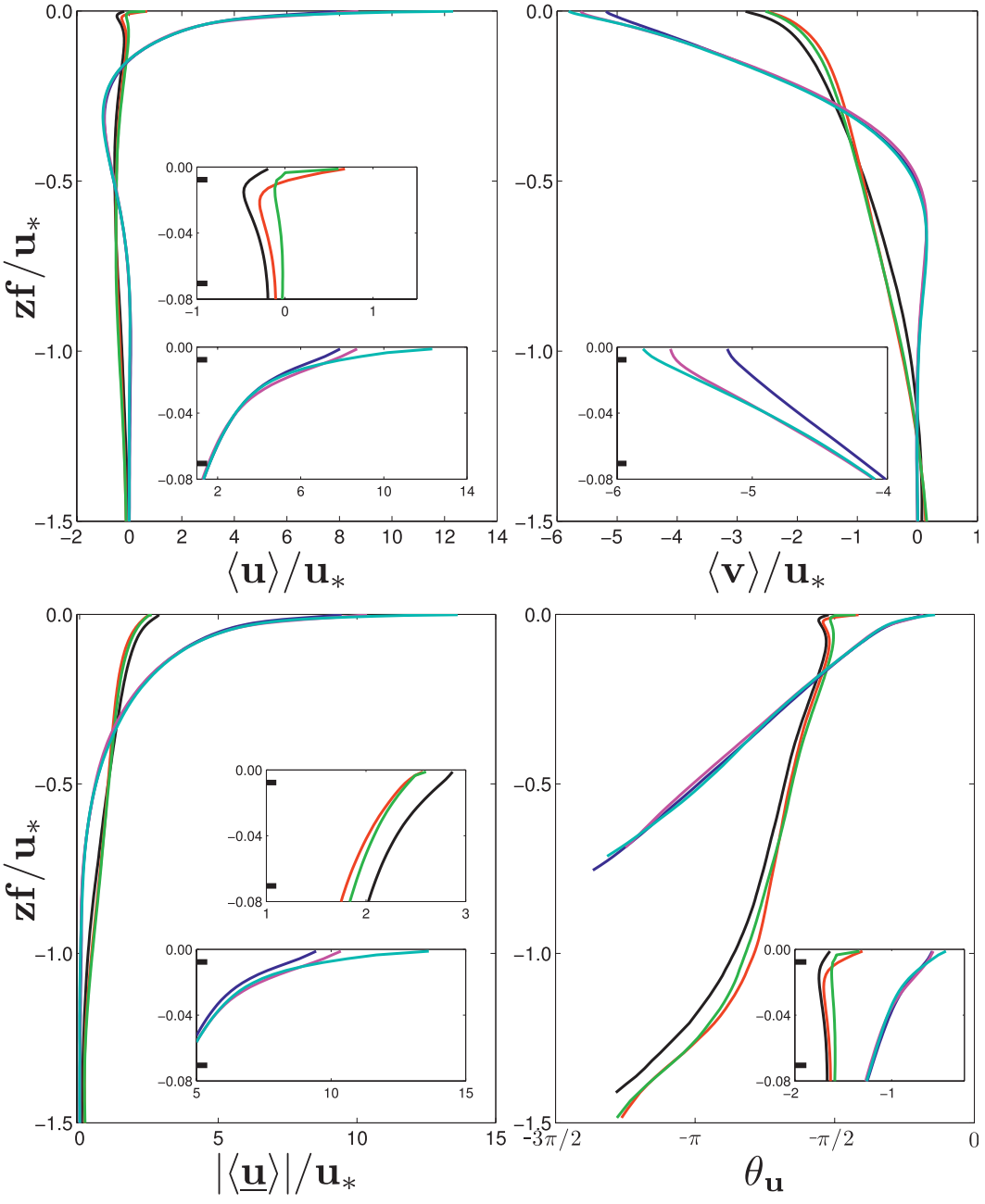

FIG. 2. Mean horizontal velocity profiles: (top) directional components normalized by u_* and (bottom) magnitude and angle relative to east. Inset plots show detail near the surface. The two thick tick marks in the insets indicate nondimensional h_{st} and h_b. All cases in Table 1 are included. The line color convention is $N\tau$ (cyan), $N\langle B\rangle$ (magenta), NB (blue), $S\tau$ (green), $S\langle B\rangle$ (red), and SB (black).

one. The vertical integrals of (3) relate the mean transport to the Stokes transport and the mean wind stress in τ cases (or its integral equivalent $\int \langle A\rangle\, dz$ in B cases),

$$\int \langle u\rangle\, dz = -\int u_{st}\, dz, \quad \int \langle v\rangle\, dz = -\frac{\tau^x}{\rho_o f}. \tag{5}$$

These relations are independent of the profiles of turbulent Reynolds stress.

The mean horizontal velocity profiles, $\langle \mathbf{u}_\perp\rangle(z) = (\langle u\rangle, \langle v\rangle)\ (z)$, have the familiar Ekman spiral structure of decaying amplitude and rotating clockwise with increasing depth (Fig. 2). The profiles for the different cases are primarily distinguished by Stokes drift effects,

with the forcing mechanism secondary. Compared to an Ekman layer without waves, Stokes drift causes the boundary layer depth h_o to be deeper (Table 1); hence, the mean velocity magnitude is diminished near the surface to satisfy the transport constraint (5). Stokes drift further diminishes the downwind velocity near the surface. This effect is a consequence of the Stokes-Coriolis force (Huang 1979): that is, the second term in the y-momentum balance in (3). It adds an anti-Stokes component to the x transport in (5) and makes the surface current angle $\theta_u(0)$ more nearly southward, $-\pi/2$. The reduced value of $\langle u\rangle(0)$ with $u_{\rm st}$ leads to the reduced energy injection rate $\mathcal{E}^{\rm tot}$ in case $S\tau$ with stress forcing (Table 1); in the cases with breaker forcing, $\mathcal{E}^{\rm tot}$ is dominated by the subgrid-scale injection $\langle W\rangle$, hence is not sensitive to $\langle u\rangle(0)$. Near the surface $\langle u\rangle(z)$ has downwind, down-wave shear. Without $u_{\rm st}$, this extends over the whole upper half of the layer, and it is especially large within a thin layer with stress forcing (as expected from Monin–Obukhov similarity, with $\langle u\rangle \sim 1/z$) controlled in the LES by the subgrid-scale mixing. Breaker forcing limits the strength of the near-surface shear over a vertical scale of h_b. With $u_{\rm st}$, the positive x shear is confined within the breaker layer h_b. Just below in the Stokes layer, the x shear is up-wave over most of the Stokes depth scale $h_{\rm st}$ in accord with the anti-Stokes tendency in (3). Even with wave effects, $\partial_z\langle v\rangle(z)$ does not have strong features on the scales of h_b and $h_{\rm st}$. With breaker forcing its surface boundary condition of zero, shear is approached within a thin layer controlled by subgrid-scale mixing. The magnitude of $\partial_z\langle v\rangle(z)$ is diminished with $u_{\rm st}$ because h_o is bigger while the y transport is the same. Overall, the oscillations with depth of the velocity component profiles (i.e., Ekman spiral) are less evident with $u_{\rm st}$ even in the interior shear layer (cf. appendix B). In both components breaker forcing and $u_{\rm st}$ cause reduced mean shear near the surface compared to surface stress forcing, and more so in the transient B cases than in the mean $\langle B\rangle$ cases, consistent with enhanced vertical momentum mixing by wave-induced breakers and LCs and the absence of a Monin–Obukhov similarity layer.

The Reynolds stress profiles, $\langle \mathbf{u}_\perp w\rangle(z)$ (Fig. 3), are grossly similar among the different cases except within the breaker layer near the surface. As with the mean velocity in Fig. 2, we plot the Reynolds stress as its magnitude $|\langle \mathbf{u}_\perp w\rangle|$ and angle θ_{-uw}. The latter is in the direction opposite to $-\langle \mathbf{u}_\perp w\rangle$ to facilitate comparison with the mean shear $\partial_z\langle \mathbf{u}_\perp\rangle$, which can be compared within the framework of an eddy viscosity assumption of proportionality between Reynolds stress and mean shear (section 3d).

The Reynolds stress angle profiles show monotonic clockwise rotation with depth by a total amount $\Delta\theta_{-uw} \approx -\pi$ before the stress magnitude becomes very small. So, the main intercase difference is due to the larger vertical scale h_o with $u_{\rm st}$. hence a slower rotation rate. In all cases, the bulk rotation rate is $d\theta_{-uw}/dz \approx -0.7\pi/h_o$. The Ekman spiral has a simpler manifestation in Reynolds stress than in mean velocity, where the anti-Stokes tendency partly obscures the rotation. Here $\langle \mathbf{u}_\perp w\rangle(0) = \partial_z\langle \mathbf{u}_\perp\rangle(0) = 0$ with breaker forcing, whereas the latter quantity is nonzero and equal to $-u_*^2$ in the x direction with stress forcing. The different surface boundary conditions for surface stress and breaker forcing are accommodated within the thin breaker layer h_b without otherwise much difference in the interior; that is, $-\partial_z\langle uw\rangle$ stays positive to the surface with eastward stress forcing while

$$-\partial_z\langle uw\rangle \approx -\langle A\rangle < 0 \tag{6}$$

with breaker forcing. Notice in particular the opposite signs between downwind Reynolds stress and mean shear within the Stokes layer (top-left panels in Figs. 2 and 3), with $\partial_z\langle u\rangle < 0$ while $-\langle uw\rangle > 0$, which is inconsistent with downgradient momentum flux; this presages the invalidity of conventional eddy viscosity parameterization in the Stokes layer (section 4). Without the Stokes-Coriolis and vortex forces, the flux is downgradient in the upper ocean and even throughout the interior shear layer (section 4). In both the upper ocean in no-wave cases and in Stokes layers, $\langle v\rangle < 0$ (mean flow to the right of the surface wind) and $\partial_z\langle v\rangle < 0$; hence, $-\partial_z\langle vw\rangle > 0$ and $-\langle vw\rangle > 0$ because of zero transverse Reynolds stress at the surface. These $\langle v\rangle$ and $\langle vw\rangle$ profiles are qualitatively similar in shape with or without waves, with the transverse Reynolds stress divergence in (3) balanced in the upper part of the layer by either $f\langle u\rangle$ or $fu_{\rm st}$ in N or S cases, respectively.

c. Velocity variance and energy balance

Many previous studies show that the Stokes drift vortex force increases e and alters the anisotropic partition of variance among the fluctuation velocity components by reducing the downwind component u' and increasing the transverse and vertical components (v', w') as expected from the idealized geometry of LCs as longitudinal roll cells. In these aspects, we also see two groupings based on whether $u_{\rm st}$ is included (S cases) or not (N cases) (Fig. 4). The cases with different forcing specifications have more complicated distinctions: τ forcing enhances u' variance and diminishes (v', w') variance near the surface without $u_{\rm st}$ (N cases) and vice versa with $u_{\rm st}$ (S cases); e is much

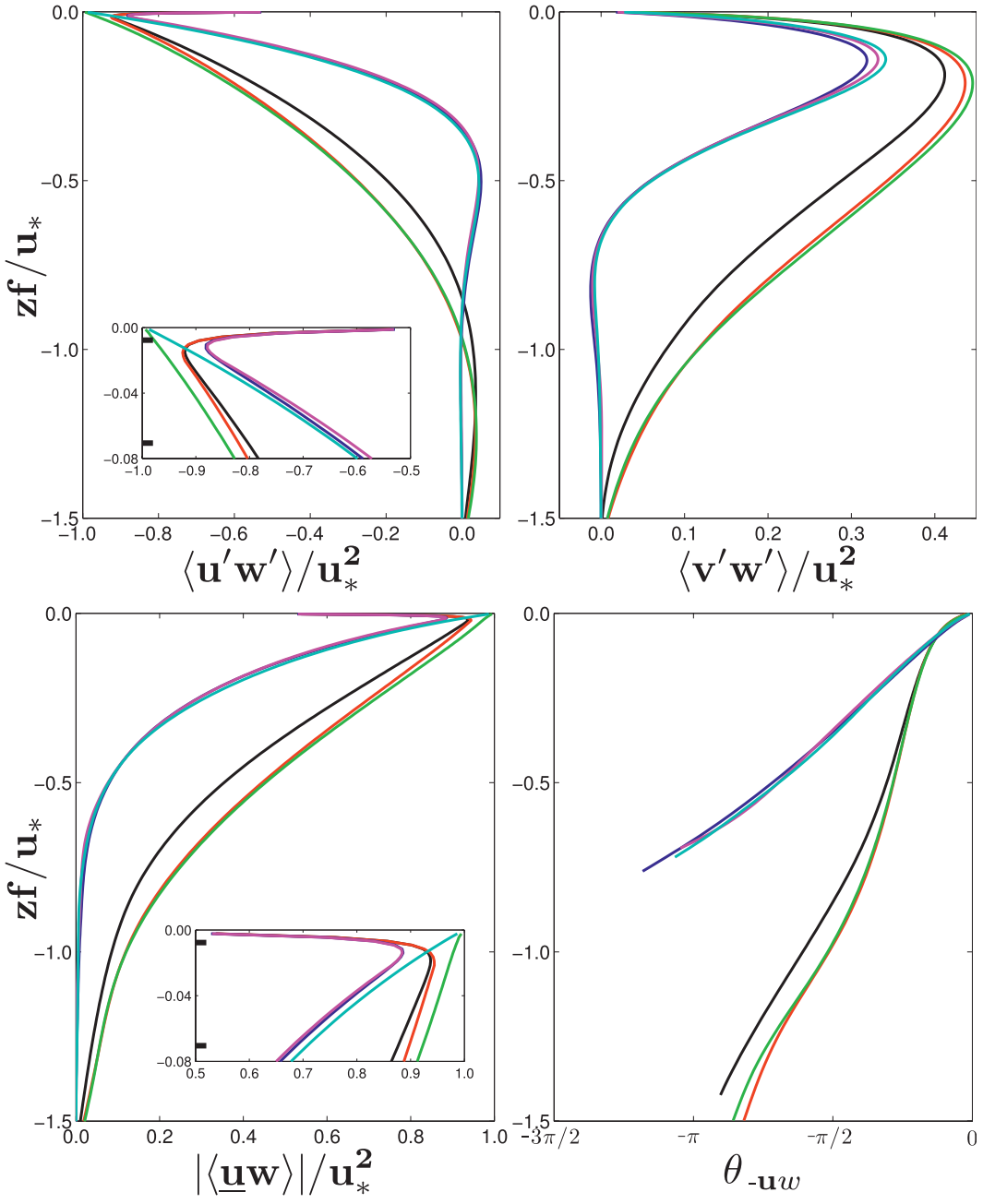

FIG. 3. Mean profiles of turbulent vertical Reynolds stress: (top) directional components and (bottom) magnitude (normalized by u_*^2) and angle θ_{-uw} (radians counterclockwise from east). Plotting conventions as in Fig. 2. The angle curve is truncated below where the stress magnitude is less than 2% of its near-surface value.

larger in the surface layer with breaker forcing than with stress forcing, and it is largest with $\langle B \rangle$ forcing, mainly because of a subgrid-scale e enhancement near the surface; and the forcing-induced differences are mostly confined to a thin layer of several times h_b. The maximum for $\langle w'^2 \rangle(z)$ occurs near the surface near the base of the Stokes layer but outside the primary influence of subgrid-scale mixing and breaker forcing. It is much stronger in S cases as an expression of LCs that have peak intensity in the Stokes layer (section 3e). The case $S\tau$ is anomalous in having the shallowest depth for the maximum, and it also has the largest surface extremum for $\langle v'^2 \rangle$; vortex force acts almost singularly in generating small-scale LCs near the surface, unless limited by the extra mixing associated with breaker forcing.

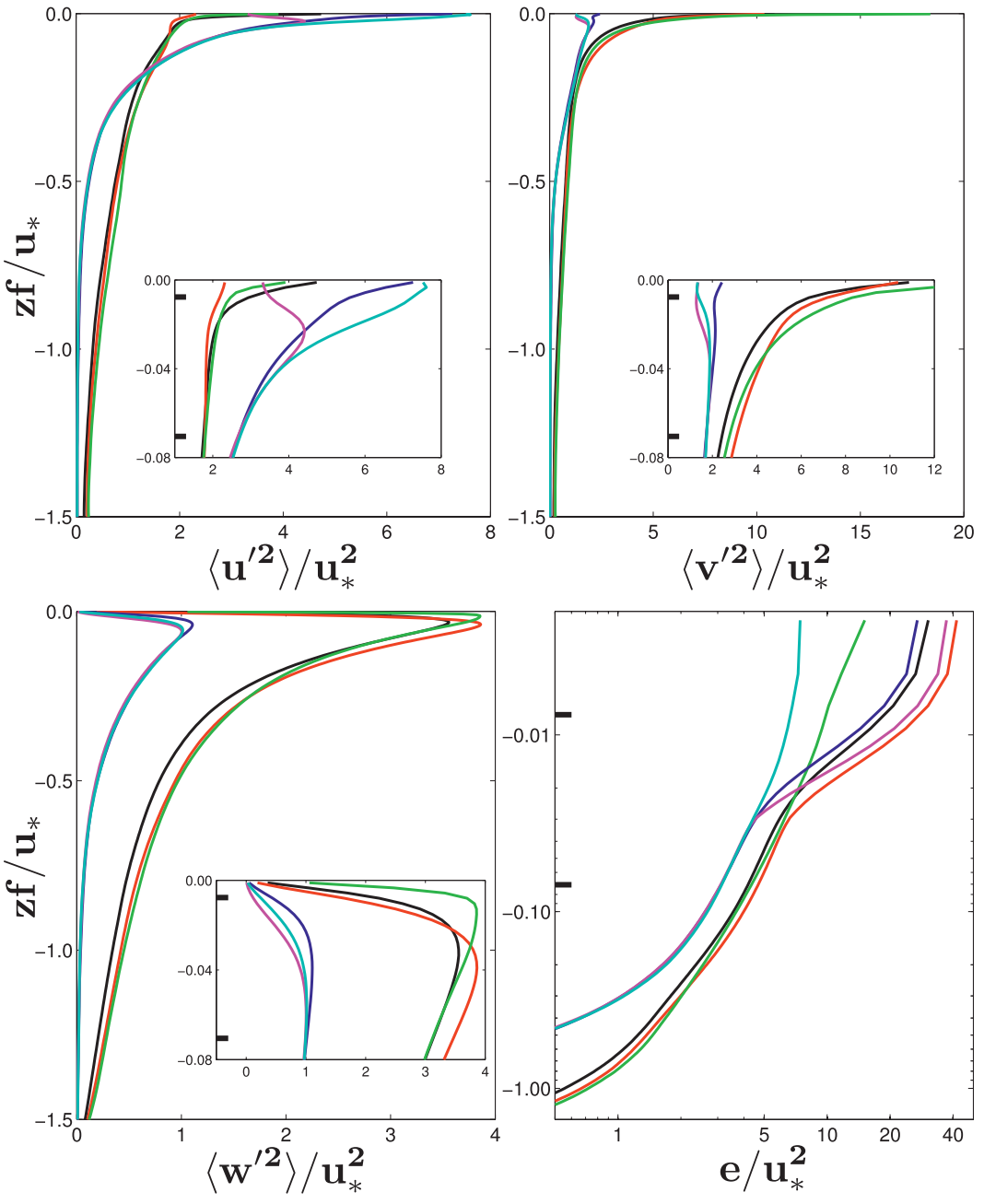

FIG. 4. Large-eddy fluctuation velocity component variances and e profiles (including the subgrid-scale energy) normalized by u_*^2. The e plot is logarithmic. Plotting conventions are otherwise as in Fig. 2.

We decompose the profile of kinetic energy into three pieces: the mean-current kinetic energy (MKE), $\overline{e}(z) = 0.5\langle \mathbf{u}_\perp \rangle^2(z)$, and the total turbulent kinetic energy (TKE), $e(z)$ in (1), which contains both large-eddy and subgrid-scale components. Energy balance relations are derived by averaging the product of the momentum equation and the velocity and adding this to an average of the subgrid-scale model that is expressed ab initio as an energy balance.

There are separate balance relations for $\overline{e}$ and e. For completeness, we record the mean energy balance in appendix A, but we focus here on the balance relation for the turbulent energy $e(z)$ in statistical equilibrium; namely,

$$\partial_t e(z) = 0 = \mathcal{E} + \mathcal{P}_u + \mathcal{P}_{st} + \mathcal{T} - \epsilon. \qquad (7)$$

The individual right side terms are transient breaker or surface wind stress work; the Reynolds stress productions

from mean shear and Stokes shear; the vertical transport; and the viscous dissipation rate, respectively. The mean wind stress $\langle\tau\rangle$ or mean breaker acceleration $\langle A\rangle(z)$ is an energy source for $\overline{e}$, not for turbulent e directly; the connection to the latter is made by a conversion through the shear production $\mathcal{P}_u$, which is thus a sink for $\overline{e}$ and a source for e (appendix A). We assume a steady wind here, which therefore does not provide a direct source for e. The transient and subgrid-scale breaker work for e is

$$\mathcal{E} = \langle A'u' + W\rangle. \tag{8}$$

The shear and Stokes production terms are

$$\begin{aligned}\mathcal{P}_u &= -\langle \mathbf{u}_\perp w\rangle \partial_z \langle \mathbf{u}_\perp\rangle \\ \mathcal{P}_{st} &= -\langle uw\rangle \partial_z u_{st},\end{aligned} \tag{9}$$

where the total horizontal Reynolds stress is defined in (4). The transport term is

$$\begin{aligned}\mathcal{T} = -\partial_z \Bigg(\Bigg\langle w' \left[\frac{1}{2}\mathbf{u}'^2 + \frac{5}{3}e^s + p'/\rho_o\right]\Bigg\rangle \\ + \langle u_i' \tau_{iz}^{s'}\rangle - 2\langle \kappa^s \partial_z e^s\rangle\Bigg)\end{aligned} \tag{10}$$

in which p is the dynamic pressure.[8] Index summation over i is implied in the next-to-last term. Finally, the viscous dissipation term occurs entirely through the subgrid-scale model,

$$\epsilon(z) = \langle \epsilon^s\rangle. \tag{11}$$

The quantities stress τ^s, energy e^s, dissipation rate ϵ^s, and eddy viscosity κ^s are local fields calculated in the subgrid-scale model (section 2).

The TKE balance without wave effects (Fig. 5, right) is a familiar story of $\mathcal{P}_u \approx \epsilon$, with $\mathcal{T}$ much weaker and acting to spread e downward from the more energetic upper part to the lower part of the Ekman layer; the crossover depth from negative to positive $\mathcal{T}$ is around 10% of h_o. The story is quite different with wave effects (Fig. 5, left). Breaker energy injection $\mathcal{E}$ now happens within the Ekman layer instead of just at the surface by wind stress work, albeit confined to the thin breaker layer h_b, and this influence is so strong that the entirety of the underlying Stokes and interior shear layers are supplied by the downward energy flux from the breaker layer, $\mathcal{T} > 0$. Dissipation ϵ is much increased in the surface layer primarily to balance the large $\mathcal{E}$, but $\mathcal{T}$ is also much increased. The transport again carries energy downward into the interior of the Ekman layer, but now $\mathcal{T}$ is positive even in the Stokes layer and at least part of the breaker layer: that is, at all depths where we trust its discrete diagnostic accuracy (see Fig. 5 caption).[9] The negative $\mathcal{T}$ values necessary for its zero depth integral are only in the top two grid cells (not plotted). Stokes production $\mathcal{P}_{\rm st}$ is much larger than $\mathcal{P}_u$ but is necessarily restricted to the Stokes layer. Within the interior shear layer $\mathcal{P}_u$ is an energy source, but small compared to transport and dissipation. Within the breaker layer, injection and transport approximately balance dissipation; over the Stokes and interior shear regions of the wavy Ekman layer, Stokes production and transport balance dissipation. The differing character of the TKE balance with depth may explain why the simple scaling estimate based on Stokes production, $u_{*\rm com}$ in (2), is not uniformly successful in accounting for wave effects (section 3a). Nevertheless, the importance of Stokes production, rather than shear production, gives support for the Lagrangian eddy viscosity proposed in sections 3d and 4.

In summary, the TKE balance without waves has shear production as its source, passed through the MKE budget from mean surface-stress wind work. In contrast, the TKE balance with waves has primarily breaker energy injection and secondarily Stokes production as its sources, both of which are conversions from the wave field; in this case the energy conversion from MKE though $\mathcal{P}_u$ is much less important. The associated MKE balances are further summarized in appendix A.

d. Eddy viscosity profiles

We diagnose the scalar eddy viscosity magnitude implied by the Reynolds stress and mean shear,

$$\kappa = \frac{|\langle \mathbf{u}_\perp w\rangle|}{|\partial_z \langle \mathbf{u}_\perp\rangle|}, \tag{12}$$

as well as directional angle defined by

[8] In LES with waves, the large-eddy pressure is

$$\pi = \frac{p}{\rho_o} + \frac{2}{3}e^s + \frac{1}{2}[(\mathbf{u} + \mathbf{u}_{\perp\rm st})^2 - \mathbf{u}_{\perp\rm st}^2]$$

(Sullivan et al. 2007). The first two terms contribute to $\mathcal{T}$ in (10), and the third term combines with the vortex force to yield $\mathcal{P}_{\rm st}$ and cancel any net contribution to $\mathcal{T}$.

[9] An implication of the diagnosed transport profile is that there probably is finescale structure on a scale of perhaps 10 cm or less near the surface, which is not well resolved in our present solutions. Besides the discretization accuracy limitation that could be ameliorated with finer grid resolution, we would question the physical validity of our subgrid-scale and breaker parameterization schemes in a surface microscale realm.

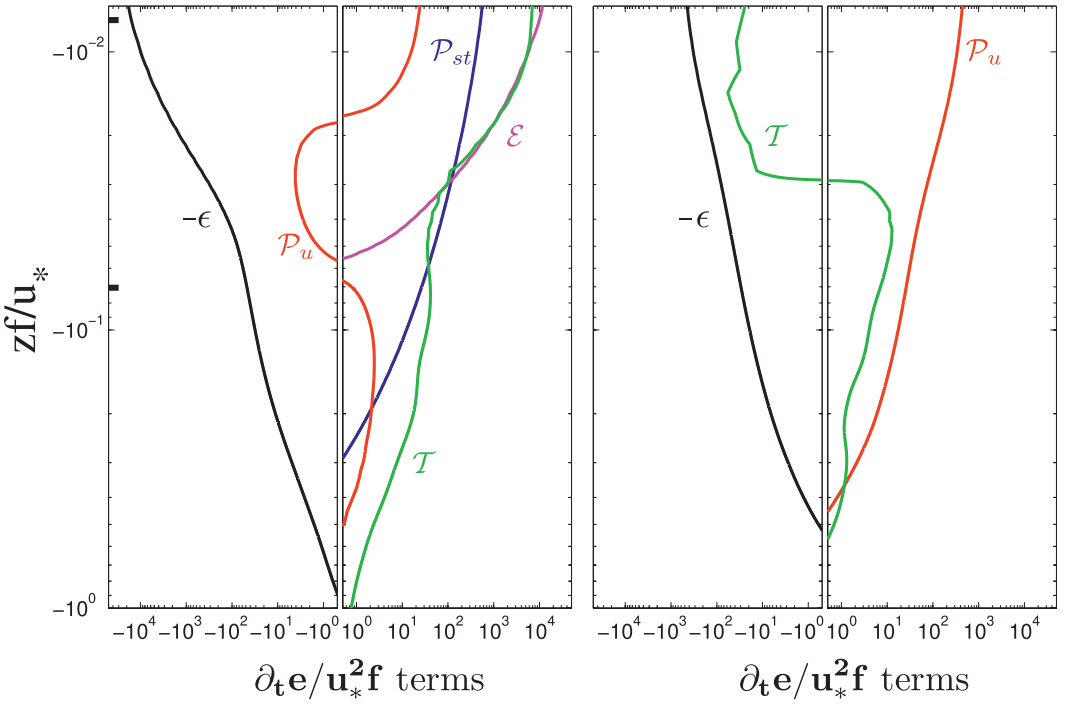

FIG. 5. TKE balances for cases (left) *SB* and (right) $N\tau$ normalized by $u_*^2 f$ on a split log–log scale, where the sign of the axis quantities is listed explicitly. Individual terms in (7)–(11) are breaker work $\mathcal{E}$ (magenta), shear production $\mathcal{P}_u$ (red), Stokes production $\mathcal{P}_{\rm st}$ (blue), transport $\mathcal{T}$ (green), and viscous dissipation $-\epsilon$ (black). Tick marks indicate $z = -h_{\rm st}$ and $-h_b$ in (left). The top two grid cells are excluded where the discretization accuracy of the TKE diagnosis is dubious as judged from the residual of rhs terms in (7).

$$\theta_\kappa = \theta_{-uw} - \theta_{u_z}, \tag{13}$$

which represents the local misalignment of the stress and shear. The usual conception of local eddy viscosity assumes that the Reynolds stress $\langle \mathbf{u}_\perp w\rangle$ is oppositely aligned with the mean shear $\partial_z\langle \mathbf{u}_\perp\rangle$, hence that $\theta_\kappa = 0$.

In an Ekman layer without wave effects in case $N\tau$, $\kappa(z)$ has a convex profile that extends over the whole of h_o (and even somewhat beyond), and $\theta_\kappa(z)$ is small (Fig. 6).

These characteristics are supportive of a full-turbulence [a.k.a. Reynolds-averaged Navier–Stokes (RANS)] eddy-viscosity parameterization scheme such as KPP, and the skill of this turbulence model is assessed in section 4. In fact, $\theta_\kappa(z)$ is slightly positive except at the boundary layer edges[10], but not to such a degree that an eddy-viscous KPP solution is inaccurate (section 4).

With wave effects in case *SB*, $\kappa(z)$ is much larger and extends deeper. Both features are qualitatively consistent with Ekman layer scalings of $h_o \sim u_{*\rm com}/f$ and $\kappa \sim u_{*\rm com} h_o \sim u_{*\rm com}^2/f$ using the composite velocity scale $u_{*\rm com}$ in (2). However, the κ enhancement is by nearly a factor of 10 in Fig. 6, while the enhancement of $(u_{*\rm com}/u_*)^2$ is not even half as large, so there is a quantitative discrepancy. A much bigger discrepancy is a large positive spike of θ_κ in the Stokes layer and a broader, but lesser, maximum in the interior of the Ekman layer. This presents a significant challenge to a conventional eddy viscosity RANS parameterization.

In anticipation of the RANS parameterization discussion in section 4, we define alternative eddy viscosity profiles relative to the Lagrangian mean flow,[11] $\langle \mathbf{u}_\perp^L\rangle = \langle \mathbf{u}_\perp\rangle + \mathbf{u}_{\rm st}$:

$$\kappa^L = \frac{|\langle \mathbf{u}_\perp w\rangle|}{|\partial_z\langle \mathbf{u}_\perp^L\rangle|}, \quad \theta_\kappa^L = \theta_{-uw} - \theta_{u_z^L}. \tag{14}$$

Without $u_{\rm st}$ (e.g., in case $N\tau$), these quantities are the same as (12). They are plotted for case *SB* in Fig. 6. Near the surface κ^L is smaller than κ because the Lagrangian

[10] The small value of $\theta_\kappa(z)$ is robustly nonzero with respect to computational parameters and statistical averaging accuracy in case $N\tau$. We do not have an explanation.

[11] This is the short-time mean velocity averaged over an ensemble of parcels that move with $\dot{\mathbf{x}} = \mathbf{u}(\mathbf{x}) + \mathbf{u}_{\perp\rm st}(\mathbf{x})$ from random initial locations and release times $\mathbf{x}(t_0)$.

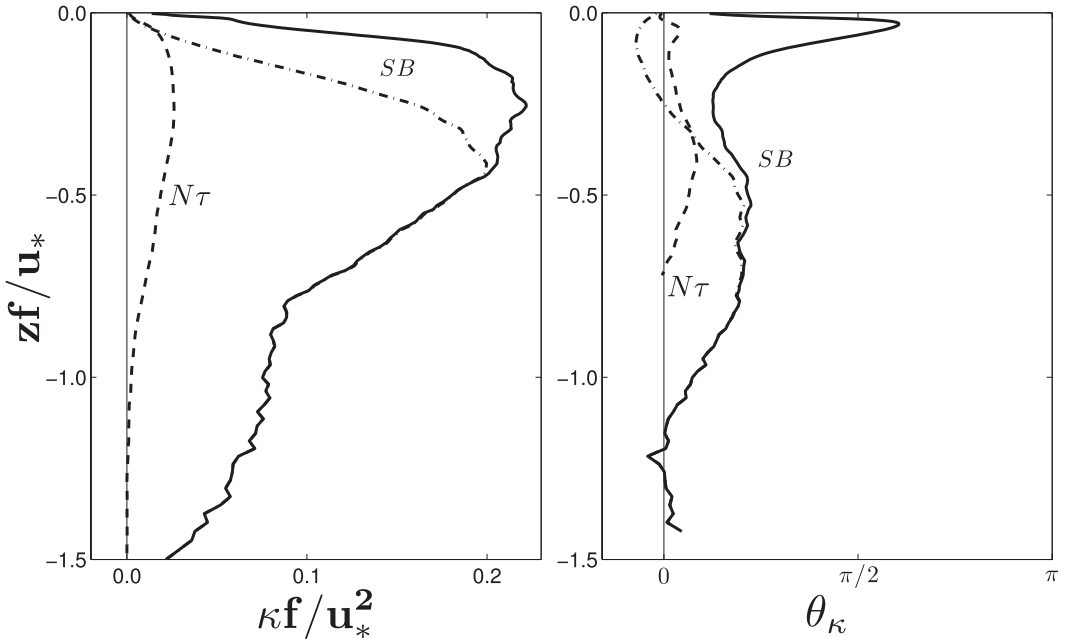

FIG. 6. Normalized eddy viscosity magnitude κ and angle θ_κ for cases *SB* (solid) and $N\tau$ (dashed). Also shown are the Lagrangian eddy viscosity and angle for the *SB* case (dashed–dotted). The curves are truncated with depth as in Fig. 3.

shear is larger, but it still is much larger than κ without wave effects.[12] The κ^L has a depth structure that is smoothly distributed over the Ekman layer h_o as a whole, and it has an evident suppression within the Stokes and breaker layers, for example, compared to a linear interpolation between the midlayer peak and the surface, which is characteristic of surface layer similarity with $\kappa \sim u_* h_o z$ when there are no wave effects. Furthermore, $\theta_\kappa^L(z)$ has a very different structure than θ_κ with a small negative lobe through the Stokes layer.[13] This suggests that an eddy viscosity parameterization based on $\langle \mathbf{u}_\perp^L \rangle$ might have more utility in the surface layer than an Eulerian one. In the interior of the Ekman layer where $u_{\rm st} \approx 0$, both the conventional and Lagrangian eddy viscosity quantities are the same. So, the interior behavior of $\theta_\kappa \approx \theta_\kappa^L > 0$ is also an issue for an eddy viscosity model. These ideas are assessed in section 4. The explanation is a slower rotation with depth of the LCs than the mean shear (section 3e).

e. Langmuir circulations

The turbulent eddies in a LES solution with vortex force have an organized LC structure, reminiscent of the well-organized longitudinal patterns often seen in surfactants in lakes and the ocean. Without $u_{\rm st}$ the eddy patterns are quite different from LCs. Figure 7 shows turbulent LCs in the vertical velocity field in case *SB*. They have smaller horizontal and vertical scales near the surface, and their longitudinal axis rotates clockwise with depth as part of the Ekman spiral. The w extrema are asymmetric with larger downward speeds than upward. This asymmetry is measured by the skewness profile, shown in Fig. 8,

$$\mathrm{Sk}[w] = \frac{\langle w^3 \rangle(z)}{\langle w^2 \rangle^{3/2}(z)}. \tag{15}$$

The effect of the vortex force (*S* cases) is to make $\mathrm{Sk}[w] \approx -0.8$ except within the breaker layer where it decreases toward zero. In contrast, the *N* cases have generally weaker skewness, especially in the upper half of the layer. The eddy patterns are more complex than the idealized roll cells of linear instability theory (Leibovich 1983). In particular, the largest $w < 0$ values occur more in

[12] The enhancement of κ near the surface is expected from a model of TKE injection by wave breaking (Craig and Banner 1994). Our solutions indicate it is an ill-determined quantity because the mean shear $\partial_z \langle u \rangle$ is weak near the surface. In contrast, κ^L is well determined; see (23).

[13] We explain $\theta_\kappa^L < 0$ in the Stokes layer by noting the Reynolds stress balance (3) if we assume is $\mathbf{u}_{\perp \rm st}$ is larger than $\langle \mathbf{u}_\perp \rangle$,

$$\langle uw \rangle \approx u_*^2 - f \int_z^0 \langle v \rangle \, dz' > 0$$

$$\langle vw \rangle \approx -f \int_z^0 u_{\rm st} \, dz' < 0:$$

$\langle vw \rangle$ decreases rapidly and θ_{-uw} rotates clockwise rapidly, while $\theta_{u_z^L}$ rotates clockwise more slowly; both effects are because $u_{\rm st}$ is relatively large.

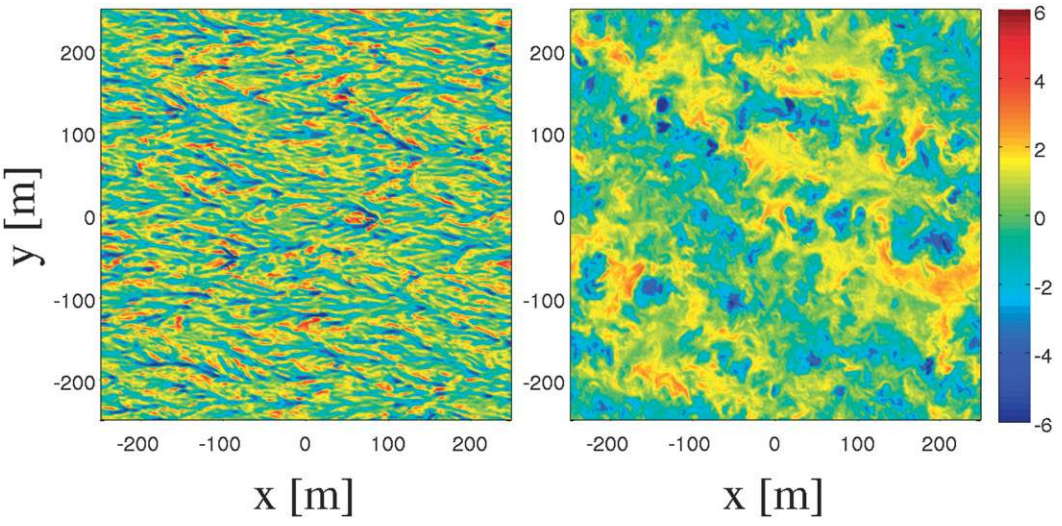

FIG. 7. Snapshots of w/u_* at depths of (left) 3 m and (right) 32 m for case *SB*.

isolated horizontal patches than along lines, although the elongated structure is evident at a lower amplitude.

To educe the typical structure of a LC, a composite average of many individual events is employed. The vertical column is divided into 14 zones with central depths z_c to aggregate LCs with similar vertical structure; the z_c are nonuniformly spaced to capture the finer scales near the surface. To detect a LC, a trigger criterion is defined to identify its central location. A normalized vertical velocity, $w^\dagger = w(x, y, z)/\mathrm{rms}[w](z)$, is used to enable detection across a broad depth range because the magnitude of w varies widely (Fig. 4). The trigger criterion is that $w^\dagger$ is a local minimum with $w^\dagger < -w^\dagger_{\mathrm{cr}}$. Many snapshot 3D volumes are sampled, each temporally separated to ensure independent events. Within a snapshot volume the detected $w^\dagger$ extrema are sorted by their magnitude, largest first. When an event is detected, a 3D local volume of size $L(z_c)^2 \cdot H(z_c)$ is then used to "black out" any other nearby events to avoid redundant captures.[14] All detected events in a given zone are then averaged together to produce a 3D composite spatial pattern in $\mathbf{u}_c(x, y, z)$ and a total detection number per volume $n_c(z)$ (i.e., per unit time). The horizontal mean is subtracted before calculating the composite fields.

Pattern recognition is inherently a fuzzy analysis procedure with potentially ambiguous event detections. So we deliberately choose conservatively large values for $w^\dagger_{\mathrm{cr}}$, L_c, and H_c. This errs on the side of undercounting the LC population by including only the strongest events based on a presumption that they will have the cleanest spatial structure. We also test that the results are not highly sensitive to the detection parameter choices, except in the total event number. The results shown here are for $w^\dagger_{\mathrm{cr}} = 4$ for all z_c and for blackout exclusion sizes that increase linearly with depth, $L_c = H_c = 2.5\ \mathrm{m} - 0.3z_c$, to match the increasing LC size (Fig. 7); for example, at the deepest $z_c = -0.95u_*/f = -177$ m, $L_c = 0.29u_*/f = 53$ m. The LC detection results in Figs. 9–11 are based on 80 temporal snapshots, with a total of 11 600 detected events used in the composite averages.

An example of a composite LC is Fig. 9 for a relatively shallow $z_c = -8$ m. It has a clean spatial structure of an elongated downwelling center along a horizontal axis rotated clockwise from the breaker direction, with weaker peripheral upwelling centers to the sides. The horizontal flow is forward along the rotated axis, with confluence in the rear and diffluence in front. Figure 9 (left) is in the plane of the $w^\dagger$ minimum, and it shows approximate fore–aft symmetry in the horizontal flow.[15] In a vertical cross section perpendicular to the axis, the primary extrema[16] in

[14] More precisely, we focus on excluding LCs with excessive lateral or vertical overlap by defining the black-out volume of a candidate LC as the union of two rectangular volumes of sizes $(2L_c)^2 \cdot H_c$ and $L_c^2(2H_c)$ each centered on the $w^\dagger$ extremum.

[15] In planes above the LC center, the afward confluent flow is much stronger than the foreward diffluent flow, especially at the surface (also see section 3.g).

[16] Because we base the detection on the locally normalized amplitude $w^\dagger$, it is not guaranteed that the absolute amplitude of w_c will be largest at z_c, as it is in Fig. 9. In Fig. 11 (note the dots on the profile curves), we see that the maxima in $|w_c|$ and κ_c occur at shallower depths than z_c for the deepest detection zones, although these maxima are deeper than for those for shallower detection zones. For the shallowest zones, the profile maxima occur slightly above z_c.

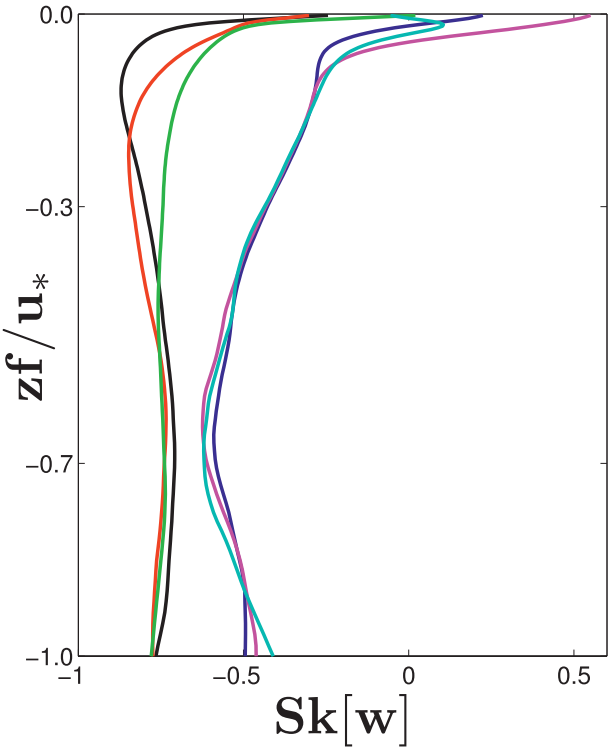

FIG. 8. Profiles of vertical velocity skewness, Sk[w](z) defined in (15), for the same set of cases using the same color coding as in Fig. 2.

$w_c < 0$ and $\tilde{u}_c > 0$ occur at $z = z_c$ (a tilde denotes a horizontally rotated quantity; see Fig. 9 caption), with approximately the same cross-axis and vertical scales that are somewhat smaller than $|z_c|$. Cross-axis horizontal convergence occurs above the central depth, and divergence occurs below. These characteristics are as we expect for LCs, although the along- and cross-axis correlation lengths are not very large in a turbulent Ekman layer.

The detected LC population density n_c is shown in Fig. 10, together with the vertical distribution of zone centers z_c and zone boundaries. The zone size expands with depth roughly matching the increase in size of the detected LCs. The n_c decreases with depth: there are fewer, bigger LCs deeper within the Ekman layer.

The average momentum flux associated with a LC composite in a zone is defined by

$$\langle \mathbf{u}_{\perp c} w_c \rangle(z) \equiv \frac{1}{\mathcal{A}} \int\int dx\, dy\, \mathbf{u}_{\perp c}(x,y,z,z_c) w_c(x,y,z,z_c), \tag{16}$$

where $\mathcal{A}$ is the horizontal area of the domain. We use its direction at $z = z_c$ to define the horizontal rotation angle $\theta_{-u_c w_c}$ used in Fig. 9; this direction is aligned with the breakers in the shallowest zone and it rotates clockwise with depth (Fig. 12). From the average flux, we define a LC composite eddy viscosity magnitude and angle analogous to (12) and (13):

$$\kappa_c(z) = \frac{|\langle \mathbf{u}_{\perp c} w_c \rangle|}{|\partial_z \langle \mathbf{u}_\perp \rangle|}, \quad \theta_c(z) = \theta_{-u_c w_c} - \theta_{\partial_z u}. \tag{17}$$

Analogous eddy-flux quantities κ_c^L and θ_c^L are defined with the Lagrangian mean shear as in (14).

The total contribution of the detected LC population to any mean quantity is equal to the product of population density n_c times the horizontal average of the composite quantity, summed over all zones. For example, the contribution to the vertical velocity variance profile is $\langle w^2 \rangle(z) = \Sigma_c n_c \langle w_c^2 \rangle$ with $\langle w_c^2 \rangle(z, z_c) = \mathcal{A}^{-1} \int\int dx\, dy\, w_c^2(x,y,z,z_c)$. Similarly, the contribution to the momentum flux is $\Sigma_c n_c \langle \mathbf{u}_{\perp c} w_c \rangle$, and the contribution to the eddy viscosity is $\Sigma_c n_c \kappa_c$. Figure 11 shows both the individual composite-zone and composite-total contributions to the $\langle w^2 \rangle(z)$ and $\kappa^L(z)$ profiles. In both quantities all zones show a similar shape varied by the peak magnitude and depth scale. So, the composite-total profiles have a similar shape. Furthermore, they are essentially similar in shape to the LES total profiles but with a smaller magnitude. The relative magnitude is somewhat larger for κ^L than for $\langle w^2 \rangle$, indicating that LCs are more efficient agents in momentum flux than their variance fraction would imply. We conclude that the statistical structure of Ekman layer turbulence is primarily the result of its coherent LCs. Because of the conservative design of the detection procedure to avoid false detections, we interpret the magnitude discrepancy as a consequence of an undercount of the LC population (n_c too small). We hypothesize that this discrepancy would close with a more sophisticated detection procedure.

A striking result in Fig. 6 is the positive eddy viscosity directions, $\theta_\kappa(z) \approx \theta_\kappa^L(z) > 0$, through the interior of the Ekman layer; that is, the clockwise rotation with depth of the Reynolds stress direction lags that of the mean shear direction (cf. Figs. 2, 3). This is alternatively shown in Fig. 12, with the addition of the Reynolds stress direction angle for the LC composite total $\theta_{-u_c w_c}$. Both Eulerian and Lagrangian shear angles differ substantially from the flux angle $\theta_{-u_c w_c}$. Near the surface the Eulerian shear is rotated far too much, while the Lagrangian angle is much closer but rotated too little. In the interior both shear angles are rotated too much, consistent with positive θ_κ and inconsistent with simple eddy viscosity. The LC composite flux angle is very close to the total flux angle near the surface. In the interior the rate of clockwise rotation is very small for the LC flux, and over the bottom half it rotates too slowly compared to the total flux. We conclude that the detected LCs are the source

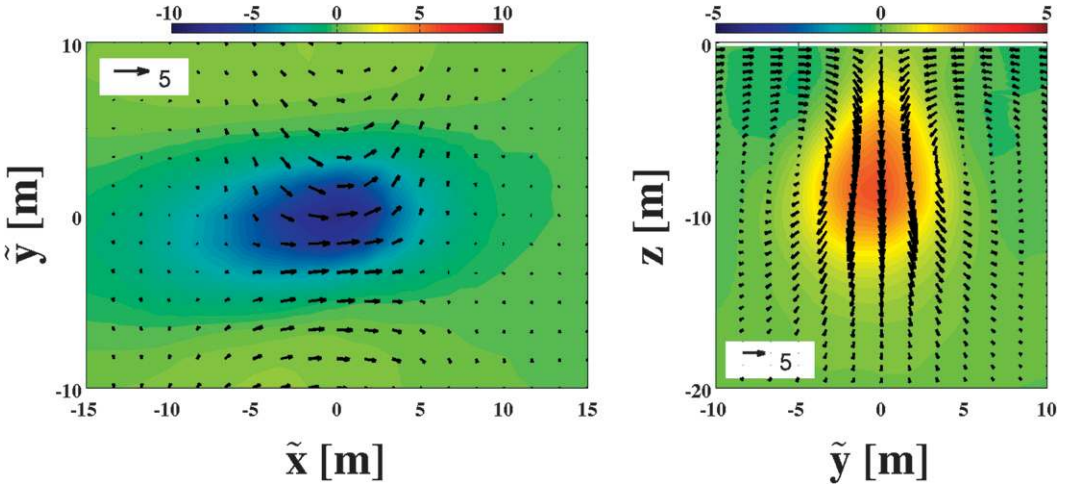

FIG. 9. (left) Composite LC pattern for case *SB* plotted in a rotated plane $(\tilde{x}, \tilde{y})$ at $z = z_c = -8$ m. The grid rotation is to the opposite direction from the horizontally averaged composite stress at the zone center z_c, $\theta_{-u_c w_c}$, whose value here is -0.18 rad. The colors show w_c/u_*, and $\tilde{\mathbf{u}}_{\perp c}/u_*$ is shown as vectors. The magnitude scale is indicated in the inset. (right) Composite LC pattern in a rotated $(\tilde{y}, z)$ plane at $\tilde{x} = 0$. The colors show $\tilde{u}_c/u_*$, and the $(\tilde{v}_c, w_c)/u_*$ velocities are shown as vectors.

of positive θ_κ. Evidently the remainder of the turbulent fluctuations (including undetected weaker LCs) have a more rotated flux angle on average, so the total flux angle value lies in between the LC flux and mean shear values. At the bottom of the Ekman layer ($z < -h_o$), all four angles coincide, but, of course, there is not much mean flow, variance, or flux down there.

f. Breakers and downwelling jets

To illustrate the 3D structure of a typical breaker, another composite average is constructed from many transient events in case *SB*. The detection criterion is that the surface u in the breaker direction exceeds a positive threshold value $U_{\rm cr}$, chosen as $U_{\rm cr} = 10u_* = 0.2$ m s^{-1}, over a connected area of $\mathcal{A}_{\rm cr} = 1.6 \times 10^{-3} (u_*/f)^2 = 55$ m^2. Again, these choices are conservative ones that select the larger, stronger breakers. For composite averaging, the origin is placed at the position of maximum $u > 0$. The composite pattern in Fig. 13 has strong downwelling in the front and weaker upwelling in the rear. The horizontal velocity is stronger in u than in v, divergent and confluent in the rear, and convergent and diffluent in front. The depth scale is slightly larger than h_b because the composite is for relatively larger, stronger breakers. Notice that the y scale is wider for breakers than for upper-ocean LCs (Fig. 9). All of these characteristics are a response to the specified shape of the breaker acceleration events, $A(x, y, z, t)\hat{\mathbf{x}}$ (Sullivan et al. 2007). As with the LC composites, the composite breaker has a Reynolds stress with $\langle uw \rangle(z) < 0$ near the surface ($z > -2h_b$); however, it is much weaker than for the LC composites.

In the wavy Ekman layer, an interesting phenomenon emerges: namely, coherent, downward-propagating, downwelling jets. We detect them by a variant of the LC detection procedure (section 3e): for a large $w^\dagger < 0$ anomaly first detected within the top 3.5 m, a search is made for another large anomaly in the local spatial neighborhood at a subsequent time 20 s later. If the new detection is successful, the process is continued in time, always

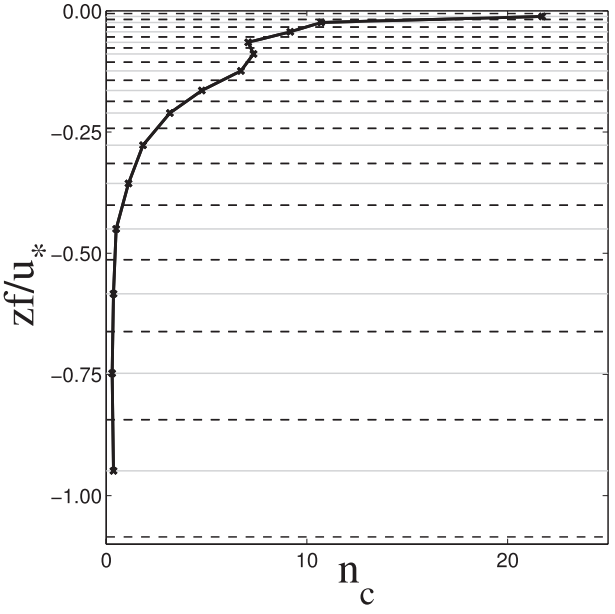

FIG. 10. Number of LC detections n_c per unit time within the domain for each vertical detection zone. Horizontal lines indicate zone centers (gray) and zone boundaries (dashed).

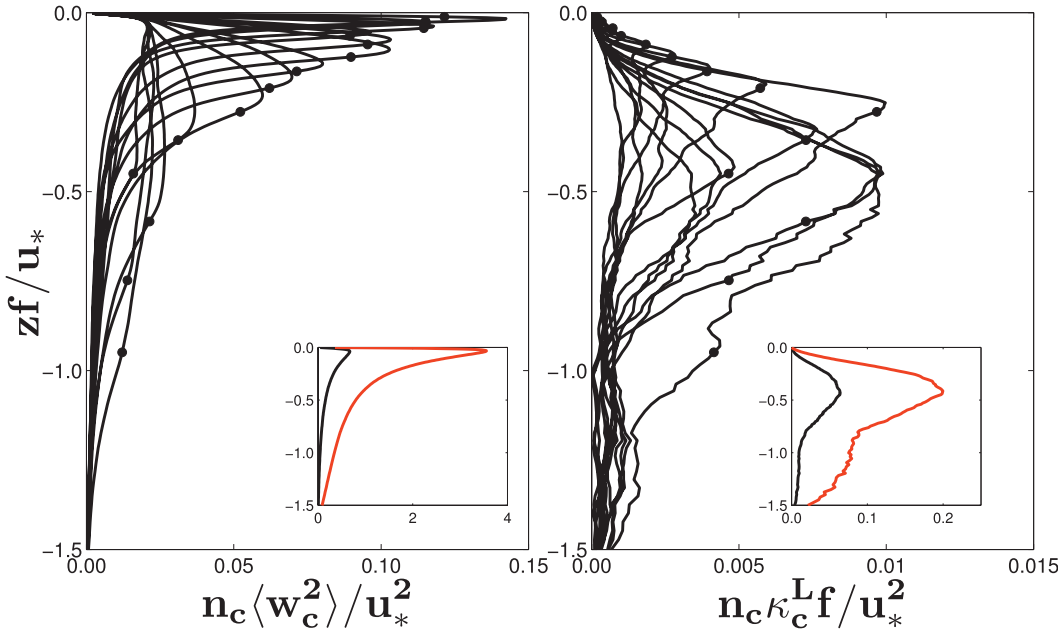

FIG. 11. (left) Normalized LC composite $n_c\langle w_c^2\rangle$ and (right) Lagrangian eddy viscosity magnitude $n_c\kappa_c^L$ for case *SB*. Separate curves are for different detection zones, with the zone center marked by a dot. The inset plots show profiles for the composite summed over all zones (black) compared to the LES total profiles (red).

searching in the local neighborhood of the latest detection. The detection sequence is terminated when no new local strong anomalies are found. This procedure yields many examples of downwelling jets that penetrate much of the way through the boundary layer (Fig. 14). They have a typical downward propagation speed of about $0.3u_*$, which is a small fraction both of the rms w (Fig. 4) and of their own local w extremum and have a typical horizontal propagation speed of several times u_*, generally following the mean flow (Fig. 2). The downwelling jet extremum typically occurs along the horizontal axis of a LC; hence, it contributes to the LC structure in w more as an isolated extremum along the axis than as a longitudinally uniform distribution typical of roll cells (Fig. 7). Deep downwelling jets are much less frequently detected than either breakers or LCs separately, but they are much more frequent and coherent in case *SB* than any of the other cases in Table 1. In laboratory experiments on breaking waves without evident LCs, deep downwelling jets are not seen (Melville et al. 2002).

Case *SB* also has the largest negative skewness among all the cases here, with $\mathrm{Sk}[w] \approx -0.85$ around $z = -0.15u_*/f$ (Fig. 8), although its distinction from other *S* cases abates into the interior. We interpret this as an incremental effect of the strong downwelling jets on top of the primary LC asymmetry in w. Thus, the jets arise out of an interaction between breakers and LCs through a vertical vorticity catalyzation process provided to LCs by the finite transverse scale of the breaker acceleration, in particular the opposite-signed vertical vorticity extrema on either side of the breaker center in Fig. 13 (left). A vertical vorticity seed is tilted and stretched by

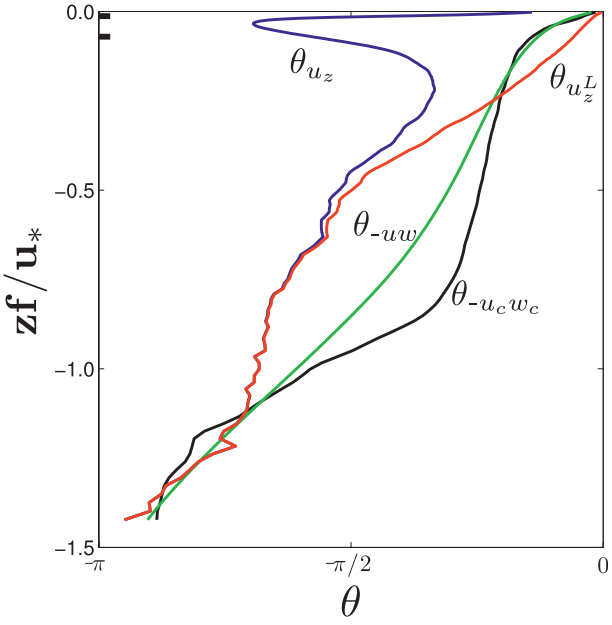

FIG. 12. Comparison of depth profiles for mean angles for case *SB*: Reynolds stress angle θ_{-uw} (green); Eulerian shear angle θ_{u_z} (blue); Lagrangian shear angle $\theta_{u_z^L}$ (red); and Reynolds stress angle from the LC composites $\theta_{-u_c w_c}$ (black). Black tick marks indicate $z = -h_b$ and $-h_{\mathrm{st}}$.

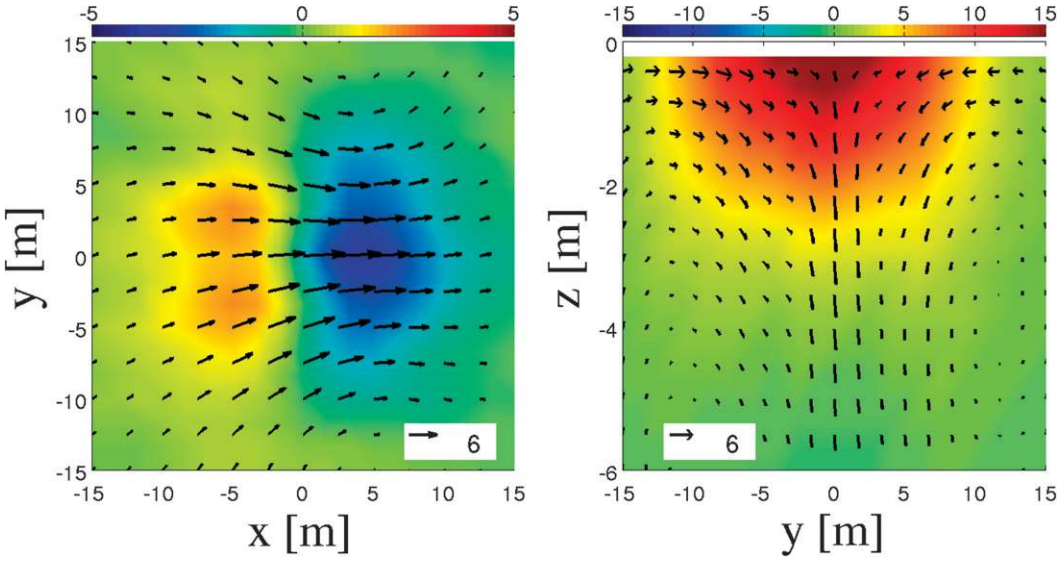

FIG. 13. Composite-average velocity in breaking waves for case *SB*. The plotting conventions are the same as in Fig. 9, except the horizontal grid is not rotated here. The horizontal plane is at $z = -1.9$ m, and the vertical section is at $x = 0$ relative to the breaker center.

Stokes drift and the mean current to grow into the longitudinal vorticity of a mature LC (Leibovich 1983; Sullivan et al. 2008). This phenomenon is more pronounced with our choice of relatively young wave age with its larger breakers than with the older waves in full wind wave equilibrium (section 2). This catalyzation process is not, of course, the only way to generate a LC because many other vertical vorticity seeds are present in a turbulent boundary layer.

g. Surface drift

A long-standing, practical oceanic question is the lateral drift of a buoyant object at the surface. Its simplest posing is as pure fluid drift, neglecting windage and other bulk forces on the object and surfactant rheological complexity. In the Ekman problem, we have defined the Lagrangian mean flow by $\langle \mathbf{u}_\perp^L \rangle = \langle \mathbf{u}_\perp \rangle + \mathbf{u}_{\rm st}$. This is the velocity of an ensemble of randomly placed particles, averaged over short time periods before their spatial distribution becomes organized. However, Langmuir turbulence is famous for its "wind rows" with surfactants that collect in the convergence zones of LCs. Furthermore, the theoretical model of a roll cell as a paradigm for a LC has a downwind surface velocity maximum along the convergence line (Leibovich 1983, Fig. 3), implying a positive drift anomaly for its trapped particles that cannot follow the downwelling flow into the interior.

We ask whether an ensemble of surface-trapped particles has the same mean velocity as $\langle \mathbf{u}_\perp^L \rangle$ (0) after long drift periods. Define $\mathbf{X}(t; \mathbf{X}_0, t_0)$ as the Lagrangian horizontal coordinate of a particle released at a random location $\mathbf{X}_0$ at time t_0. For $t > t_0$ it moves with the local surface Lagrangian flow:

$$\frac{d\mathbf{X}}{dt} = \mathbf{u}_\perp(\mathbf{X}(t), 0, t) + \mathbf{u}_{\rm st}(0). \tag{18}$$

(This is a wave-averaged trajectory that excludes orbital motion of surface gravity waves.) The long-time surface drift $\mathbf{U}^L$ is defined as the ensemble average of (18) over many releases at $(\mathbf{X}_0, t_0)$ and their $\mathbf{X}(t)$ trajectories of long duration. Figure 15 (left) is a snapshot for the wavy case *SB* of a set of $\mathbf{X}(t)$ positions with a large $t - t_0$, calculated by (18) using LES $\mathbf{u}_\perp$ fields. The locations are organized into fragmented lines and apparently have lost any correlation with their original release locations by becoming trapped in convergence zones. For this case the mean drift velocities expressed in (u, v) components are $\langle \mathbf{u}_\perp^L \rangle = (17.3, -2.9)u_*$ and $\mathbf{U}^L = (17.1, -3.3)u_*$, with a large downwind $u_{\rm st}(0) = 17.5u_*$ contribution. So, the short- and long-term Lagrangian drifts are relatively little different.[17] Similarly small differences are seen in our other LES cases.

We calculate the composite-average surface horizontal flow conditioned on strong convergence (Fig. 15, right). There is little horizontal flow through the convergence center, which is where surface trajectories will spend most

[17] Nevertheless, their differences are statistically significant based on standard error estimates. Across the *S* cases, the long-term drift is rotated more to the right than the short-term drift [i.e., $\hat{\mathbf{y}}(\mathbf{U}^L - \langle \mathbf{u}_\perp^L \rangle) < 0$].

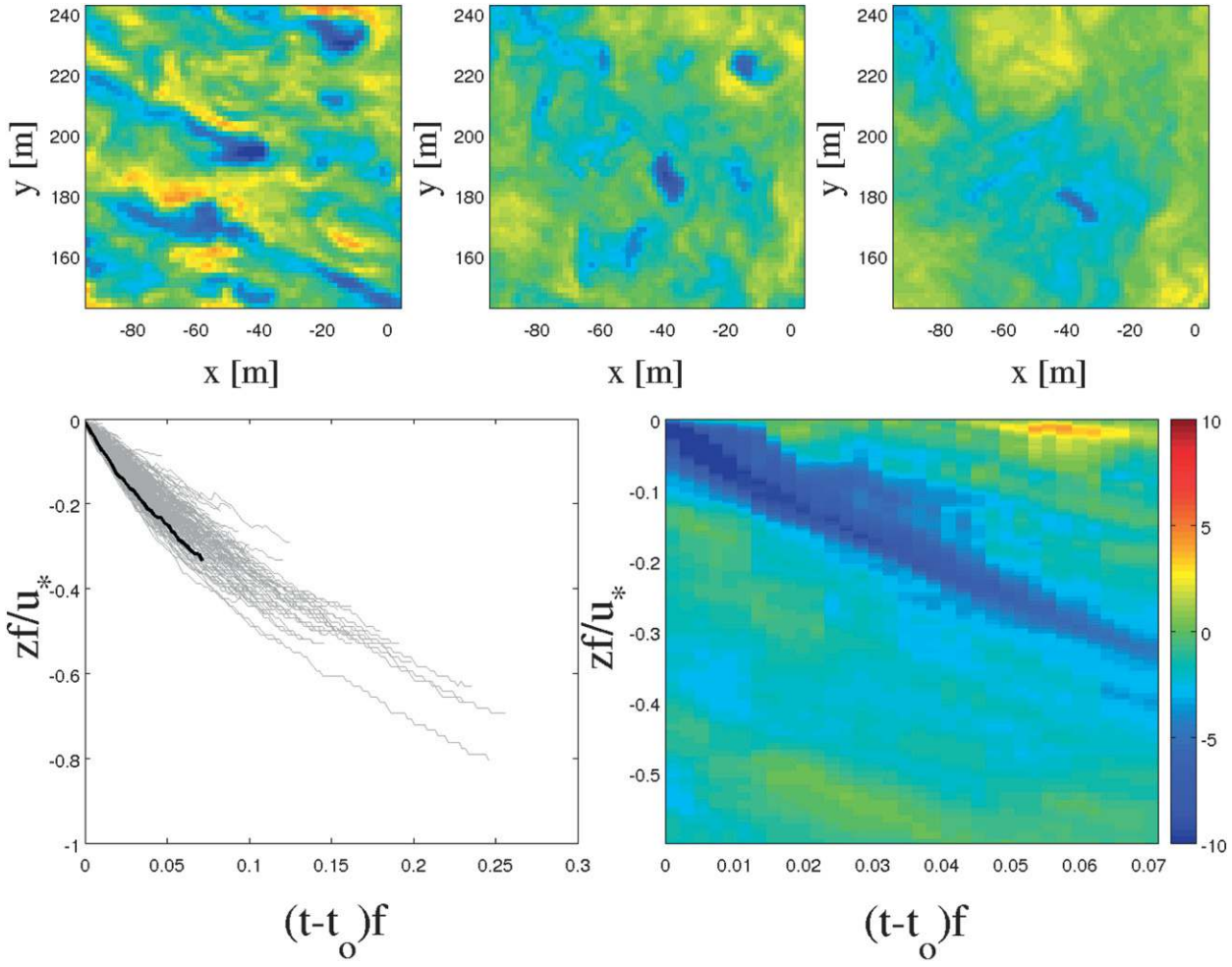

FIG. 14. Examples from case *SB* of deep jets emanating from near the surface at their first detection time t_0: (bottom left) Hovmöller diagram in (z, t) of many jet centers (gray lines) with one particular jet trajectory (in black) selected for the other panels here; (bottom right) $w(z, t)/u_*$ following the black trajectory at the horizontal location of its center; and (top) snapshots of $w(x, y)/u_*$ for the same trajectory at depths of 10, 30, and 50 m with relative time separations of 190 and 270 s, using the same color bar.

of their time once they become organized into wind rows. That is, the surface-trapped particles move into the LCs but do not move through them. A similar fore–aft asymmetry for surface flow in the LCs is shown for hurricane LES simulations with nonequilibrium wind waves in Figs. 11 and 12 of Sullivan et al. (2012) though with some instances of nonzero but weak down-axis flow ahead of the downwelling center. This flow structure contradicts the roll-cell paradigm with a positive downwind velocity anomaly extending along the cell axis. However, it does partly explain why $\mathbf{U}^L$ and $\langle \mathbf{u}_\perp^L \rangle$ are nearly the same in our LES solutions; that is, at the surface particles and LC convergence patterns move at approximately the same speed on average as the overall Lagrangian mean flow. [At the subsurface level of maximum downwelling in a LC, the down-axis flow is positive though the cell (e.g., Fig. 9), but this is not where particles are trapped.] Weller and Price (1988) measures large positive downwind velocity anomalies near the LC convergence lines (their Fig. 8a), which they interpret as consistent with the roll-cell paradigm; however, because they cannot precisely collocate their velocity measurements with surface particle trajectories, it is not clear that this contradicts our results.

Using the u_*–U_a relation in section 2, we can re-express the mean drift velocity $\langle \mathbf{u}_\perp^L \rangle \approx \mathbf{U}^L$ as about $0.02U_a$ rotated 10° to the right of the wind direction for case *SB*. In the ocean an ensemble of surface drift measurements is difficult to control for varying conditions of wind, waves, and stratification, and commonly averages are made by lumping different situations together. Ardhuin et al. (2009) uses a combination of surface radar backscatter and a numerical wave model to estimate mean surface drifts (comparable to $\langle \mathbf{u}_\perp^L \rangle$ because they would not see particle trapping) of 0.01–018 U_a rotated 10°–40° to the

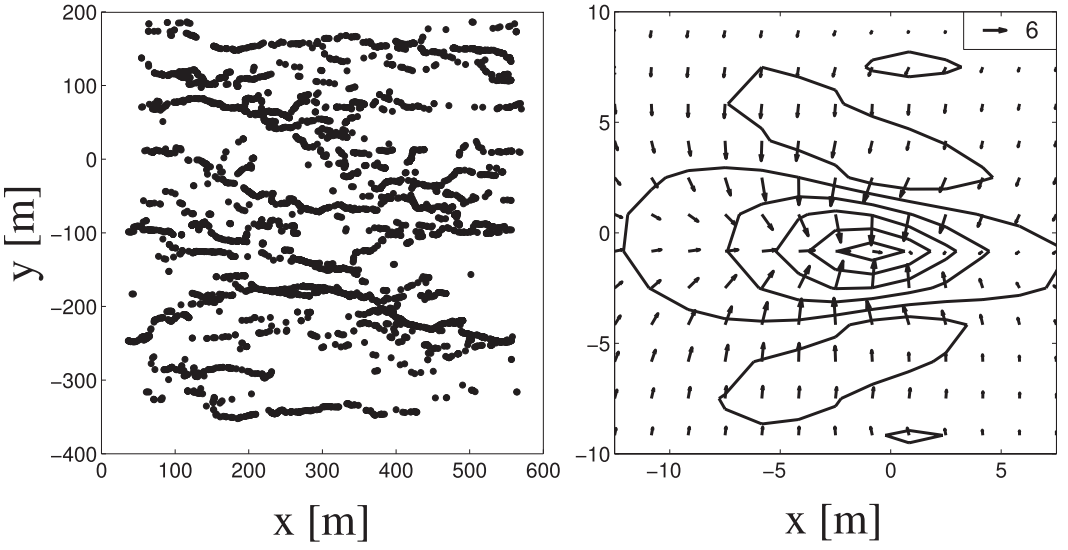

FIG. 15. (left) Snapshot of 5000 surface particle locations $\mathbf{X}$ at a time $t - t_0 = 10^3$ s $= 0.1\, f^{-1}$ after random releases within the (x, y) domain between ± 250 m in each direction. Notice the spreading and mean eastward and southward drifts. (right) Composite-average surface velocity anomaly vectors, $(\mathbf{u}_\perp(x, y) - \langle \mathbf{u}_\perp \rangle)/u_*$ (arrows), conditioned on a surface convergence extremum by a procedure otherwise similar to the breaker detection in section 3f. The composite-average convergence fields are contoured with an interval of $0.02\, f^{-1}$, with a central maximum of $0.1\, f^{-1}$. The surface velocity anomaly is nearly zero at the center of convergence. These plots are for case *SB*.

right of the wind, with higher speed and greater rotation when the stratification is strong. They explain that their speed may be an underestimate because some depth averaging is implicit in the radar backscatter process near the surface where the Stokes shear is large. Given this caveat and their lumping of many situations, we do not see our answer for $\mathbf{U}^L$ as notably inconsistent. However, there is a literature of empirical estimates of substantially larger surface drift speeds in excess of $0.03U_a$ (e.g., Bye 1966; Wu 1983; Kim et al. 2009), which is not supported by our LES results or by the measurements of Ardhuin et al. (2009); we will not attempt to reconcile these historical contradictions.

4. Parameterization implications

Oceanic general circulation models (OGCMs) require full-turbulence (RANS) parameterization of boundary layer turbulent fluxes to calculate upper ocean currents and material distributions. Because $\langle \mathbf{u}_\perp \rangle\ (z)$ is quite different in cases *SB* and $N\tau$ (Fig. 2), we conclude that presently used OGCM parameterizations are inadequate without wave effects. In particular, the parameterization influences on boundary layer depth, vertical mixing rate, and velocity profile shape need to be changed.

A 1D RANS parameterization model for the Ekman layer with uniform density is a turbulence-averaged momentum equation for $\mathbf{u}_\perp(z, t)$ with specified wind and wave forcing in the x direction [τ^x, $u_{\rm st}(z)$, and $A(z)$]:

$$\frac{\partial \mathbf{u}}{\partial t} + f\hat{\mathbf{z}} \times (\mathbf{u} + u_{\rm st}\hat{\mathbf{x}}) = A\hat{\mathbf{x}} + \frac{\partial \mathbf{F}}{\partial z}, \tag{19}$$

where $\mathbf{F}$ is the parameterization of the Reynolds stress, $-\langle \mathbf{u}_\perp w \rangle(z)$. Boundary conditions are $\mathbf{F} = (\tau^x/\rho_o)\hat{\mathbf{x}}$ at $z = 0$ and $\mathbf{u}_\perp$, $\mathbf{F} \to 0$ as $z \to -\infty$. The KPP model for the unstratified Ekman layer is

$$\begin{aligned} \mathbf{F}(z) &= \kappa(z)\frac{\partial \mathbf{u}_\perp}{\partial z} \\ \kappa(z) &= c_1 u_* h G(\sigma), \quad \sigma = -\frac{z}{h}, \quad h = c_2\frac{u_*}{f} \\ G(\sigma) &= \sigma(1-\sigma)^2, \quad \sigma \le 1,\ G = 0,\ \sigma > 1, \end{aligned} \tag{20}$$

with constants c_1 and c_2 (McWilliams and Huckle 2006). Notice that there are no wave influences in this scheme for $\mathbf{F}$.

We test KPP for the classical Ekman layer without wave effects: that is, case $N\tau$. First, we optimally fit the values of c_1 and c_2 to minimize $\mathcal{R}$, the depth-integrated rms difference in $\mathbf{u}_\perp(z)$ between LES and KPP, normalized by the rms magnitude of $\mathbf{u}_\perp(z)$ from LES. The minimum value is $\mathcal{R} = 0.1$ for $c_1 = 0.29$ and $c_2 = 0.72$. These constants are close to the values $c_1 = k = 0.4$ for the von Kármán constant k and $c_2 = 0.7$ previously

proposed for an Ekman layer modeled with KPP (viz., McWilliams and Huckle 2006) but with c_1 somewhat smaller here. The quality of the KPP fit to $\mathbf{u}_\perp(z)$ is good by boundary layer parameterization standards (Fig. 16). There are larger discrepancies in the shape of $\kappa(z)$ than in $\mathbf{u}_\perp(z)$, but eddy viscosity itself is not the important parameterization product for OGCMs except as a means to obtain $\mathbf{u}_\perp$. In particular, without stable density stratification, κ in LES does not vanish at depth as sharply as in the KPP model, but the deep value of κ is evidently not very important in determining $\mathbf{u}_\perp(z)$ after it has decayed to a small magnitude. What is most important for achieving a small value of $\mathcal{R}$ is matching the surface layer structure where $\mathbf{u}_\perp$ is large. The KPP recipe (20) is consistent with a wall-bounded similarity layer (a.k.a. log layer) where $\kappa \to c_1 c_2 u_*^2/f|z|$ as $|z| \to 0$; thus, the strongest constraint is on matching the product of $c_1 c_2$ with the LES answer. A caution is that the similarity-layer shear is theoretically singular, $\partial_z u \to k u_*/z$; hence, LES can only provide a discretely approximate standard for such a case, and LES–1D discretization differences also limit the degree of agreement in $\mathbf{u}_\perp$. The modest degree of nonalignment between $\langle \mathbf{u}_\perp w \rangle$ and $\partial_z \langle \mathbf{u}_\perp \rangle$ ($\theta_\kappa > 0$ in Fig. 6 for case $N\tau$) is evidently not a serious obstacle to a reasonably skillful fit with the KPP parameterization scheme. By practical parameterization standards for use in OGCMs, there is little motivation to try to do better in this wind-only case, apart from improving the precision of the calibration and OGCM implementation if these are important limitations.

The comparative analyses with and without wave effects indicate that $\mathbf{u}_\perp(z)$ is substantially altered by waves (section 3). At the least, the boundary layer depth needs to be deeper and the eddy viscosity κ magnitude be larger with wave effects (Table 1 and Fig. 6). McWilliams and Sullivan (2000) propose an amplified κ magnitude due to $u_{\rm st}$ based on a case with a stratification-limited depth, and Eq. (2) suggests a scaling for the amplification of the turbulent velocity scale[18] (but note the cautionary remark at the end of section 3a). Figure 6 shows $\theta_\kappa > \pi/2$ for case *SB* around the Stokes layer. In a conventional relation of aligned flux and shear, $\mathbf{F} = \kappa \partial_z \mathbf{u}$, this implies locally negative diffusion, which is potentially ill behaved in time integration of the 1D model (19). Recognizing the existence of flux-gradient misalignment in LES with waves, Smyth et al. (2002) propose the addition of non-eddy-viscous, countergradient flux profiles to a KPP scheme for $\mathbf{F}$, in analogy with its successful application in a convective regime (where $\partial_z \langle T \rangle$ and $\langle wT \rangle$ have the same sign over much of the boundary layer). This proposal has the disadvantage of complexity by needing to specify a model for the vector profile shape and orientation and, unlike in the convective regime, the eddy momentum flux here is not literally countergradient (i.e., $\theta_\kappa \neq \pi$). A potentially simpler remedy to the ill behavior of a negative-diffusion scheme is suggested by the alternative of a stress-aligned Lagrangian eddy viscosity scheme,

$$\mathbf{F} = \kappa^L \partial_z \mathbf{u}_\perp^L \tag{21}$$

with $\kappa^L \geq 0$. Figure 6 shows that the problematic Stokes layer structure in θ_κ is greatly diminished in θ_κ^L in case *SB*.

To assess the 1D representation of the wave effects, we solve (19) with the $\langle A \rangle(z)$ and $u_{\rm st}(z)$ profiles from Fig. 1 and a replacement for $\mathbf{F}$ with the generalized Lagrangian eddy viscosity profiles $\kappa^L(z)$ and $\theta_\kappa^L(z)$ defined in (14):

$$\mathbf{F} = \kappa^L \mathbf{R} \cdot \partial_z \mathbf{u}_\perp^L \quad \text{with} \quad \mathbf{R} = \begin{pmatrix} \cos\theta_\kappa^L & -\sin\theta_\kappa^L \\ \sin\theta_\kappa^L & \cos\theta_\kappa^L \end{pmatrix}, \tag{22}$$

where $\mathbf{R}(\theta)$ is a horizontal rotation matrix representing the rotation of the shear direction into the Reynolds stress direction. In this expression, $\kappa^L \mathbf{R}(z)$ is an eddy viscosity tensor, dependent upon two scalar functions, $\kappa^L(z)$ and $\theta_\kappa^L(z)$. Using (22), we can reproduce the LES result for $\mathbf{u}_\perp$ with good accuracy ($\mathcal{R} = 0.05$) for case *SB* using the LES-diagnosed profiles of κ^L and θ_κ^L in Fig. 6. This can also be done with an analogous Eulerian viscosity form for $\mathbf{F}$ and LES-diagnosed Eulerian viscosities.

Now we ask which aspects of the LES viscosity profiles are important by solving (19) with alternative profiles. Step 1: We refit the KPP Eq. (20) to the LES $\kappa(z)$ in Fig. 6 for a $\kappa^{L(1)}$ by matching the interior shear layer shape near its peak. This match can be done better with Lagrangian κ^L than an Eulerian κ because its peak is deeper and more in the center of the layer, as in the KPP shape. The refitted coefficients are $c_1 = 0.8$, $c_2 = 1.4$, consistent with bigger κ and h_o with waves. The resulting $\mathbf{u}_\perp(z)$ with ($\kappa^L = \kappa^{L(1)}$, $\theta_\kappa = 0$) is a very poor fit to the case *SB* profile (R = 0.8), mainly due to very different $u(z)$ near the surface. Step 1 is thus necessary but insufficient. Step 2: Noting that the $\kappa^{L(1)}$ is very much larger than the LES κ^L near the surface (because there is no similarity layer with waves), we derive a surface layer approximation to the x-momentum balance in (3) by neglecting Eulerian velocity compared to Stokes velocity in the aligned Lagrangian eddy viscosity model (21):

[18] A consequence of larger κ is increased entrainment rate at the pycnocline (McWilliams et al. 1997). This is likely to be a general behavior in stratified boundary layers with waves.

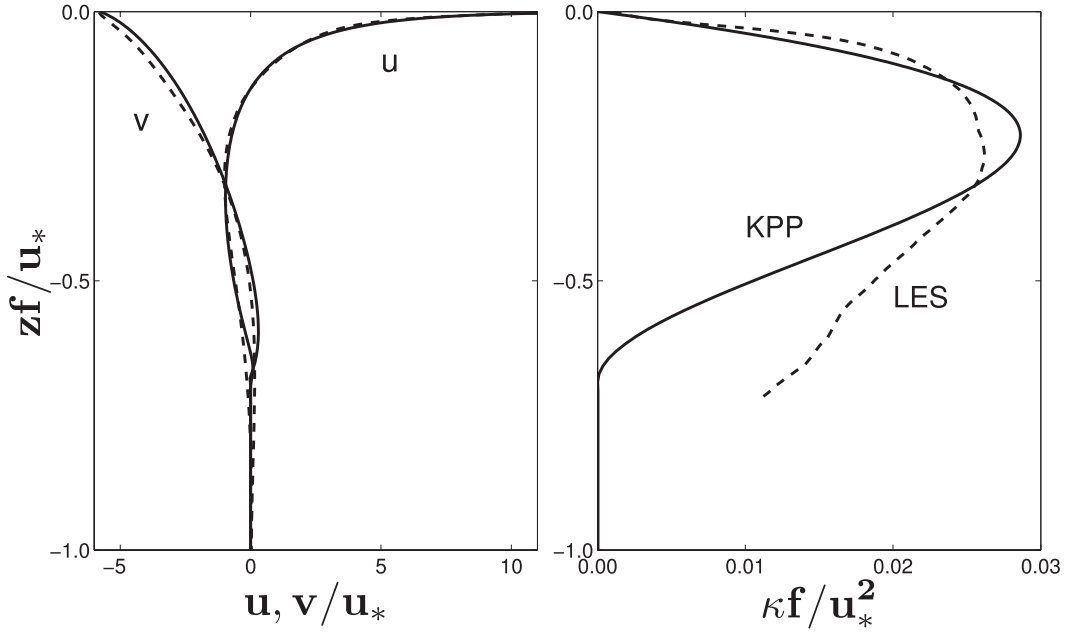

FIG. 16. Normalized profiles of (left) mean velocity $\langle \mathbf{u}_\perp \rangle(z)$ and (right) eddy viscosity $\kappa(z)$ for case $N\tau$ without wave effects, comparing the LES result (dashed) with the KPP model (20) with optimally fit constants $c_1 = 0.29$ and $c_2 = 0.72$ (solid). After the fit the rms depth-integrated relative difference in $\mathbf{u}_\perp$ between LES and KPP is $\mathcal{R} = 0.1$. $\kappa(z)$ for LES is again truncated below where the Reynolds stress magnitude is less than 2% of its near-surface value.

$$\kappa^L_{\rm sur}(z) = \frac{\int_z^0 A(z')\,dz'}{\partial_z u_{\rm st}(z) + S_o} \geq 0 \tag{23}$$

in which $\kappa^L_{\rm sur} \to 0^+$ as $z \to 0^-$ in the Stokes layer, because the denominator is increasing while the numerator $\approx u_*^2$, and even more so in the breaker layer, because the numerator is also decreasing. The S_o prevents divergence of $\kappa^L_{\rm sur}$ as $z \to -\infty$, and the small value $S_o = 0.0025\,\partial_z u_{\rm st}(0)$ makes a smooth transition in a composite specification,

$$\kappa^{L(2)}(z) = \min[\kappa^L_{\rm sur}(z), \kappa^{L(1)}(z)], \tag{24}$$

in the upper part of the boundary layer with $\kappa^{L(2)} = \kappa^{L(1)}$ in the lower part. Figure 17 shows that $\kappa^L_{\rm sur}$ and, hence, $\kappa^{L(2)}$ are an excellent fit to the LES-derived κ^L above the blending point at $z \approx -0.18u_*/f$. In the interior shear layer, $\kappa^{L(2)}$ is a modest misfit to the LES κ^L, to a similar degree as in case $N\tau$ in Fig. 16. The 1D solution for $\mathbf{u}_\perp$ with ($\kappa^{L(2)}$, $\theta^L_\kappa = 0$) has qualitatively the right profile shape (Fig. 18, left) with a moderate rms error of $\mathcal{R} = 0.27$. Here, as with case $N\tau$, the deeper reach of κ^L in LES is not important for the $\mathbf{u}_\perp$ skill. Step 3: To further reduce the error, we include the misalignment effect with the smoothed and depth-truncated $\theta^{L(3)}_\kappa(z)$ profile in Fig. 17, which has a small negative lobe in the Stokes layer and a larger positive lobe in the interior shear layer, as discussed in section 3d. This choice together with the viscosity magnitude $\kappa^L = \kappa^{L(2)}$ gives a very good fit in $\mathbf{u}_\perp(z)$ with $\mathcal{R} = 0.09$. The reduction in $\mathcal{R}$ between the second and third steps is due to both θ^L_κ lobes, with the surface lobe the more beneficial. The transition depth between the lobes of θ^L_κ is approximately the same transition depth as in (24), just below the Stokes layer.

Appendix B is the analytic Ekman layer solution for misaligned, Lagrangian eddy viscosity with constant viscosity κ_o and rotation angle θ_o. It provides an explanation for the primary differences in $\mathbf{u}_\perp(z)$ between the two panels in Fig. 18: near the surface, where $\theta^L_\kappa < 0$, u is larger and $-v$ is smaller, that is, less clockwise rotation relative to the wind direction, and in the interior shear layer, where $\theta^L_\kappa > 0$, the vertical decay length is shorter and the Ekman spiral is less pronounced. It also illustrates that there are ill-behaved solutions for θ^L_κ values too different from zero [analogous to negative diffusion with the aligned-stress model (21)].

The influence of breaker acceleration A (versus surface stress τ^x) is only weakly evident in the shape of $\mathbf{u}_\perp(z)$ in Fig. 18 as a weak positive shear in u and positive veering in θ_u (also in Fig. 2). The primary x-momentum balance in the breaker layer is between A and $-\partial_z(uw)$, not the Coriolis force $\propto fv$. The most

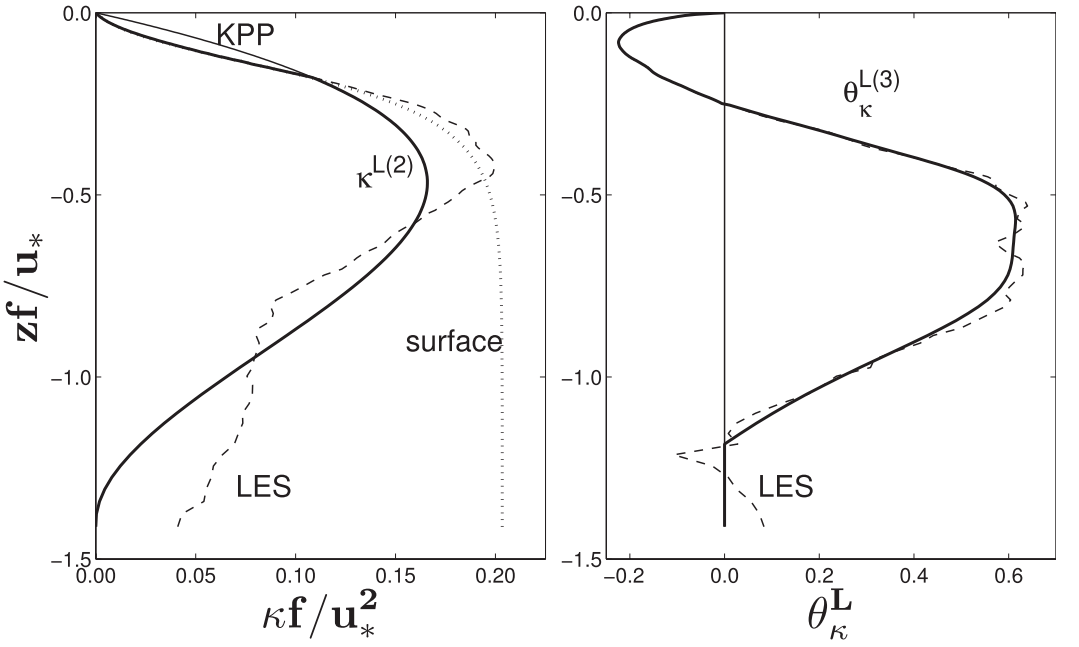

FIG. 17. Lagrangian eddy viscosity profiles for the comparisons in Fig. 18. (left) The $\kappa^L(z)$ for KPP (step 1), the surface model (23), the LES diagnostic using (14), and the blended profile $\kappa^{L(2)}$ in (24). (right) The $\theta_\kappa^L(z)$ from the LES diagnostic and a smoothed fit $\theta_\kappa^{L(3)}$ above $z \approx -1.2u_*/f$.

important A influence is a desingularization of the surface layer, compared to a surface stress boundary condition and its associated similarity layer. For $z < -h_b$ where $\int_z^0 A\,dz' = u_*^2$, all of κ^L, $\mathbf{u}_\perp$, and the Reynolds stress profiles are smooth in z, and the limiting case $h_b \to 0$ is mathematically and computationally well behaved and physically meaningful. In contrast, a surface stress condition in combination

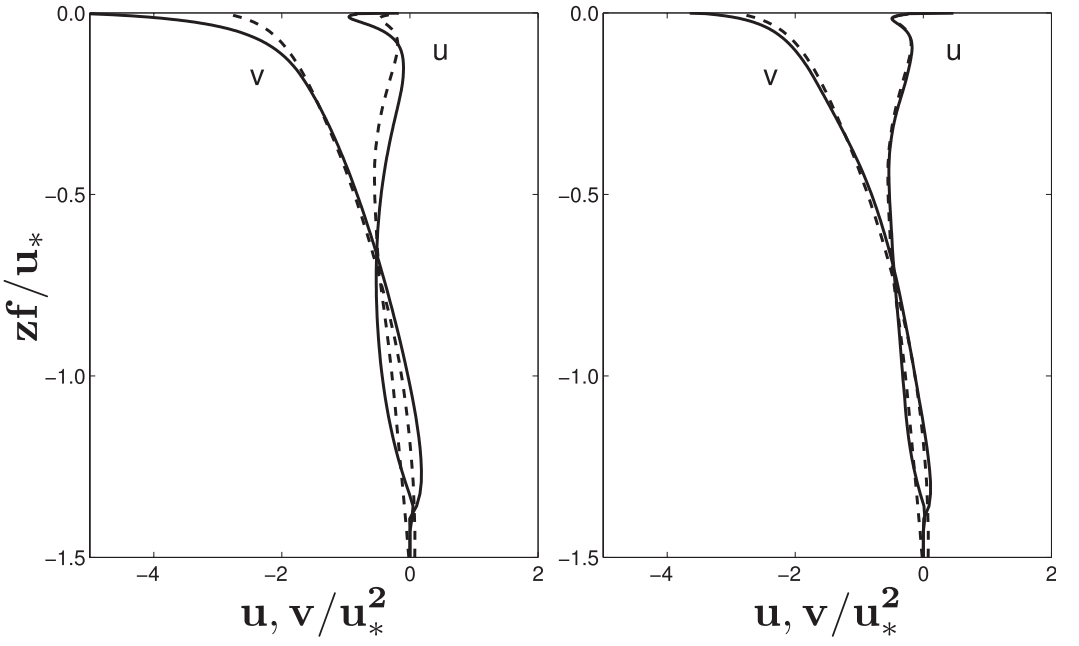

FIG. 18. Comparisons of $\mathbf{u}_\perp(z)$ for case *SB* between the LES mean and the 1D model with Lagrangian eddy viscosity: (left) steps 1–2 with $\kappa^{L(2)}$ and $\theta_\kappa^L = 0$ and (right) steps 1–3 with $\theta_\kappa^{L(3)} \neq 0$. The respective rms differences with the LES profile are $\mathcal{R} = 0.27$ and 0.09.

with $\kappa \to 0$ is ill-behaved and illconceived in the presence of waves.

Thus, we have demonstrated in three steps—the first: the familiar KPP model for the interior shear layer with a wave-enhanced κ magnitude and depth scale; and the second: a derived dynamical approximation near the surface; and the third: a qualitatively simple, albeit unfamiliar misalignment profile shape (which could easily be expressed in a formula)—that an accurate 1D model is achieved with Lagrangian eddy viscosity in the wavy Ekman regime with both τ and $u_{\rm st}$ important [i.e., $\kappa^L_{\rm sur}$ in (23) vanishes when $\tau = 0$, and its derivation assumes large Stokes shear]. This cannot be done as well with Eulerian eddy viscosity because there is no derivable analog of $\kappa_{\rm sur}$ for the Stokes and breaker layers, which therefore would have to be yet another empirically fitted aspect of the model; the Eulerian θ_κ shape is more convoluted (Fig. 6); and the fit to a KPP shape is less apt in the interior shear layer. One might argue that the first two steps alone—leaving out the $\theta^L_\kappa \neq 0$ profile specification—yield a significant improvement over existing parameterizations without wave effects. With or without the third step, this could become a useful framework for OGCM use.

This demonstration does not yet yield a usable parameterization scheme, of course, because the few LES cases examined here do not make up a regime scan of wind, wave, and buoyancy influences in the surface boundary layer,[19] with the extensive calibration and testing necessary for usability. Nevertheless, it is likely that the wave influences seen in the Ekman problem will be echoed more generally.

5. Summary

Under conditions close to wind wave equilibrium, the influences of surface gravity waves are quite significant in the Ekman layer. The Stokes-Coriolis and vortex forces are the main influences, while the differences between breaker acceleration and surface stress are secondary and mostly localized near the surface. The Ekman layer as a whole approximately separates into three vertical sublayers: the breaker layer where A is large, the Stokes layer where $u_{\rm st}$ is large, and the interior shear layer underneath, with $h_b \ll h_{\rm st} \ll h_o$ in the cases considered here. These distinctive sublayers are evident in the mean current and Reynolds stress profiles, as well as the momentum and turbulent kinetic energy balances. The Ekman layer with waves is deeper and more energetic, and its surface current profile $\mathbf{u}_\perp(z)$ is controlled by the shapes of $A(z)$ and $u_{\rm st}(z)$—neither of which is easily measured in the ocean—acting through $\kappa_{\rm sur}$ (23) and the 1D momentum balance (3) with Stokes-Coriolis force. This is a different conception of Ekman surface layer dynamics than either Monin–Obukhov similarity or breaker energy injection (Craig and Banner 1994); breaker energy injection $\mathcal{E}(z)$ does occur distributed over h_b, but it does not directly relate to the Reynolds stress $\mathbf{F}$ or eddy viscosity κ, hence not to the momentum balance and $\mathbf{u}_\perp(z)$ profile. The cases with mean acceleration and energy injection profiles, $\langle A\rangle(z)$ and $\langle W\rangle(z)$, give generally similar answers to those with stochastic A and W, and they are much simpler and more economical to compute. The energy cycle is very different with forcing by either mean stress or breaker injection so that the latter is much to be preferred as a process depiction. The partial wave formulation of Stokes drift without breaker injection (case $S\tau$) is ill structured approaching the surface, with LCs developing very fine scales without the regularization provided by breaker-augmented mixing and dissipation.

Breaker acceleration creates transverse overturning cells near the surface, and shear instability and Stokes vortex force create longitudinal LCs whose scale expands and horizontal orientation rotates with depth. Both types of coherent motions contribute important Reynolds stress. These influences occasionally combine to create downward-propagating downwelling jets. In the surface layers, the large Stokes shear requires rapid rotation with depth of the Reynolds stress, and in the interior shear layer the LCs rotate clockwise (i.e., have substantial vertical coherence) more slowly with depth than the mean shear (Ekman spiral); these behaviors create a moderate degree of stress–shear misalignment that is inconsistent with downgradient eddy viscosity. The mean surface Lagrangian drift of buoyant particles with waves is dominated by the Stokes drift velocity and rotated slightly rightward; this drift is only slightly different for short- and long-time particle trajectories in spite of particles become trapped within LC convergence zones.

To both explore parameterization possibilities and test our comprehension of wave influences, we solve a 1D model (19) with parameterized Reynolds stress $\mathbf{F}$. Without wave effects (case $N\tau$), a K-profile parameterization scheme is successful. With wave effects (case SB) several modifications are necessary for success: a KPP profile shape with greater, deeper eddy viscosity in the interior shear layer; a Lagrangian eddy viscosity scheme (23) in the breaker and Stokes layers; and a stress–shear

[19] The Coriolis force with a nonvertical rotation axis is also influential in Ekman layers, especially in the tropics. A KPP scheme is proposed in McWilliams and Huckle (2006), but as yet its interplay with wave effects is unexamined.

misalignment profile with $\theta_\kappa^L < 0$ in the Stokes layer and >0 in the interior shear layer.

The ocean has a wide range of wind wave conditions, as well as various buoyancy influences. Often the transient evolution is more evident than a steady-state equilibrium in the surface boundary layer. So, the wavy Ekman layer problem solved here, while central, is hardly general. A good strategy is still needed for encompassing the general behaviors of the upper ocean in measurements and models.

Acknowledgments. The authors are grateful to the National Science Foundation (Grant DMS-785 0723757) and Office of Naval Research (Grant N00014-08-1-0597) for support. Computations were made on the supercomputers Bluefire at the National Center for Atmospheric Research and Thresher and Trestles at the San Diego Supercomputing Center. We appreciate discussions with Fabrice Ardhuin about surface drift.

APPENDIX A

Mean and Total Kinetic Energy Balances

The energy analyses in sections 3a and 3c focus on the total work done by stress and breaker forcings, $\int \mathcal{E}^{\rm tot}\, dz$, and on the turbulent kinetic energy (TKE): e defined in (1) contains both resolved-eddy and subgrid-scale energies and its balance relation (7). To clarify the total energy context, we complement them here with the energy balance relation for the mean flow (MKE): $\overline{e} = 0.5\langle \mathbf{u}_\perp \rangle^2$. Their sum then gives a combined balance perspective for the total kinetic energy, $e^{\rm tot} = \overline{e} + e$.

In equilibrium the MKE balance relation is

$$\partial_t \overline{e}(z) = 0 = \overline{\mathcal{E}} + \overline{\mathcal{F}} + \overline{\mathcal{T}} - \mathcal{P}_u. \qquad \text{(A1)}$$

With a steady, eastward wind stress acting as a delta function at the surface ($z = 0$), the mean stress and breaker acceleration injection is

$$\overline{\mathcal{E}}(z) = \delta(z)\tau^x \langle u \rangle(0)/\rho_o + \langle A \rangle(z)\langle u \rangle(z), \qquad \text{(A2)}$$

while the fluctuating breaker acceleration A' work and subgrid-scale injection W are assigned to the e balance in (8). The Stokes-Coriolis force provides an energy conversion with the surface gravity wave field [as does Stokes production, $\mathcal{P}_{\rm st}$ in (9), for the e balance (7)]:

$$\overline{\mathcal{F}}(z) = f\hat{\mathbf{z}} \cdot \langle \mathbf{u}_\perp \rangle \times \mathbf{u}_{\perp \rm st} = -f\langle v \rangle u_{\rm st}. \qquad \text{(A3)}$$

The mean transport is

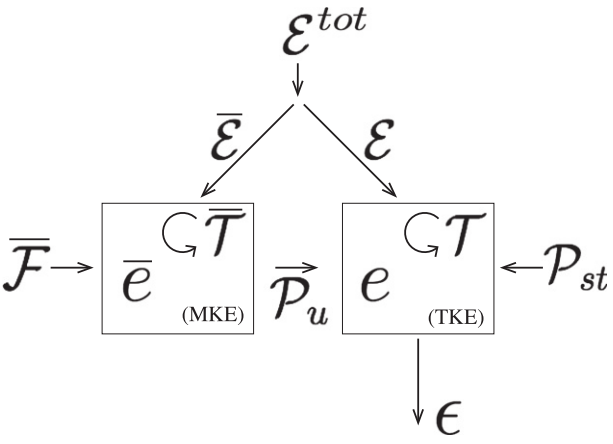

FIG. A1. Diagram of the volume-integrated turbulent and mean kinetic energy balances in (7) and (A1). Quantities are defined in the text.

$$\overline{\mathcal{T}}(z) = -\partial_z(\langle \mathbf{u}_\perp w \rangle \cdot \langle \mathbf{u}_\perp \rangle), \qquad \text{(A4)}$$

whose vertical integral is zero. The shear production $\mathcal{P}_u$ defined in (9) is a conversion from $\overline{e}$ to e. Finally, notice that a mean dissipation rate associated with the subgrid-scale stress can be defined as

$$\overline{\epsilon}(z) = -\langle \tau_{iz}^s \rangle \partial_z \langle u_i \rangle, \qquad \text{(A5)}$$

with index notation (i here is only horizontal because $\langle w \rangle = 0$); however, it is already part of $\mathcal{P}_u$ in (9), so it does not contribute separately to the MKE balance.

The total energy balance relation is the sum of (7) and (A1). It has depth-integrated sources from injection, $\mathcal{E}^{\rm tot} = \overline{\mathcal{E}} + \mathcal{E}$; Stokes–Coriolis conversion $\overline{\mathcal{F}}$; and Stokes production $\mathcal{P}_{\rm st}$ and a single dissipative sink from ϵ. This is shown diagrammatically in Fig. A1. Notice that all three sources contain a conversion with the surface wave field. The sum of sources equals the dissipation sink in equilibrium.

We do not show a quantitative evaluation of the MKE balances, but rather summarize them qualitatively from a volume-integrated perspective. With Stokes vortex forces (S cases), the primary $\overline{e}$ source is $\overline{\mathcal{F}} > 0$, and $\overline{\mathcal{E}}$ is small because $\langle u \rangle(0)$ is small, both a consequence of the Stokes-Coriolis force. [The sign of $\overline{\mathcal{F}}$ is clearly positive in (A3) because $\langle v \rangle < 0$ by the southward Ekman transport constraint in (5).] However, $\mathcal{P}_{\rm st} \gg \overline{\mathcal{F}}$ in all S cases, and $\mathcal{E}$ is even larger than $\mathcal{P}_{\rm st}$ with breakers (B cases), so the two wave conversions acting directly in the TKE balance are the important sources, with the $\mathcal{P}_u$ conversion from MKE a minor effect. The wavy energy route is summarized as $\mathcal{E} + \mathcal{P}_{\rm st} \rightarrow \epsilon$. This is very different from the Ekman layer without waves (case $N\tau$), where the MKE $\rightarrow$ TKE route is essential: $\overline{\mathcal{E}} \rightarrow P_u \rightarrow \epsilon$.

APPENDIX B

Analytic Solution with Misaligned Lagrangian Viscosity

As an aid to interpreting the 1D solutions in section 4, we pose the Ekman layer problem with Stokes-Coriolis force, a misaligned Lagrangian eddy viscosity that is uniform with depth, an equivalent surface stress boundary condition (which is well behaved for constant viscosity), and a velocity that vanishes toward the interior:

$$f\hat{\mathbf{z}}\times\mathbf{u}_\perp^L = \kappa_o\mathbf{R}(\theta_o)\partial_z^2\mathbf{u}_\perp^L$$
$$\kappa_o\mathbf{R}(\theta_o)\partial_z\mathbf{u}_\perp^L(0) = \hat{\mathbf{x}}\frac{\tau^x}{\rho_o}. \quad \text{(B1)}$$

The analytic solution is readily obtained by recasting the problem as a second-order, complex differential equation for $U = u^L + iv^L$, using $\mathbf{R} = e^{i\theta_o}$ simply as a complex number. The result for the Eulerian velocity is

$$u(z) = -u_{\rm st}(z) + \frac{\tau^x}{\rho_o\sqrt{f\kappa_o}}e^{kz}\cos\left[lz - \frac{\pi}{4} - \frac{\theta_o}{2}\right] \quad \text{(B2)}$$

$$v(z) = \frac{\tau^x}{\rho_o\sqrt{f\kappa_o}}e^{kz}\sin\left[lz - \frac{\pi}{4} - \frac{\theta_o}{2}\right] \quad \text{(B3)}$$

with vertical decay and oscillation wavenumbers,

$$k = \left(\frac{f}{\kappa_o}\right)^{1/2}\cos\left[\frac{\pi}{4} - \frac{\theta_o}{2}\right] \quad \text{and} \quad l = \left(\frac{f}{\kappa_o}\right)^{1/2}\sin\left[\frac{\pi}{4} - \frac{\theta_o}{2}\right], \quad \text{(B4)}$$

when θ_o is in a range around 0 where $k > 0$. With $u_{\rm st} = \theta_o = 0$, this is the classical Ekman solution. Otherwise, compared to the classical solution, u has a flow component opposite to $u_{\rm st}$; the vertical decay rate k is faster and the rotation rate l is slower with $\theta_o > 0$ (and vice versa if $\theta_o < 0$); and some θ_o values are inconsistent with a boundary layer solution (e.g., $\theta_o = -\pi/4$ where $k = 0$).

REFERENCES

Ardhuin, F., L. Marie, N. Rascle, P. Forget, and A. Roland, 2009: Observation and estimation of Lagrangian, Stokes, and Eulerian currents induced by wind and waves at the sea surface. *J. Phys. Oceanogr.,* **39,** 2820–2838.

Bye, J., 1966: The wave-drift current. *J. Mar. Res.,* **25,** 95–102.

Craig, P., and M. Banner, 1994: Modeling wave-enhanced turbulence in the ocean surface layer. *J. Phys. Oceanogr.,* **24,** 2546–2559.

Grant, A., and S. Belcher, 2009: Characteristics of Langmuir turbulence in the ocean mixed layer. *J. Phys. Oceanogr.,* **39,** 1871–1887.

Harcourt, R., and E. D'Asaro, 2008: Simulation of Langmuir turbulence in pure wind seas. *J. Phys. Oceanogr.,* **38,** 1542–1562.

Huang, N., 1979: On surface drift currents in the ocean. *J. Fluid Mech.,* **91,** 191–208.

Kim, S., B. Cornuelle, and E. Terrill, 2009: Anisotropic response of surface currents to the wind in a coastal regime. *J. Phys. Oceanogr.,* **39,** 1512–1532.

Kukulka, T., A. Pluededdemann, J. Trowbridge, and P. Sullivan, 2010: Rapid mixed layer deepening by the combination of Langmuir and shear instabilities: A case study. *J. Phys. Oceanogr.,* **40,** 2381–2400.

Large, W., J. McWilliams, and S. Doney, 1994: Oceanic vertical mixing: A review and a model with a non-local K-profile boundary layer parameterization. *Rev. Geophys.,* **32,** 363–403.

Leibovich, S., 1983: The form and dynamics of Langmuir circulations. *Annu. Rev. Fluid Mech.,* **36,** 391–427.

McWilliams, J., and P. Sullivan, 2000: Vertical mixing by Langmuir circulations. *Spill Sci. Technol.,* **6,** 225–237.

——, and E. Huckle, 2006: Ekman layer rectification. *J. Phys. Oceanogr.,* **36,** 1646–1659.

——, P. Sullivan, and C. Moeng, 1997: Langmuir turbulence in the ocean. *J. Fluid Mech.,* **334,** 1–30.

Melville, W., F. Veron, and C. White, 2002: The velocity field under breaking waves: Coherent structures and turbulence. *J. Fluid Mech.,* **454,** 203–233.

Moeng, C., 1984: A large eddy simulation model for the study of planetary boundary-layer turbulence. *J. Atmos. Sci.,* **41,** 2052–2062.

Polton, J., and S. Belcher, 2007: Langmuir turbulence and deeply penetrating jets in an unstratified mixed layer. *J. Geophys. Res.,* **112,** 1646–1659.

——, D. Lewis, and S. Belcher, 2005: The role of wave-induced Coriolis-Stokes forcing on the wind-driven mixed layer. *J. Phys. Oceanogr.,* **35,** 444–457.

Skyllingstad, E., and D. Denbo, 1995: An ocean large eddy simulation of Langmuir circulations and convection in the surface mixed layer. *J. Geophys. Res.,* **100,** 8501–8522.

Smyth, W., E. Skyllingstad, G. Crawford, and H. Wijesekera, 2002: Nonlocal fluxes and Stokes drift effects in the K-profile parameterization. *Ocean Dyn.,* **52,** 104–115.

Sullivan, P., and J. McWilliams, 2010: Dynamics of winds and currents coupled to surface waves. *Annu. Rev. Fluid Mech.,* **42,** 19–42.

——, ——, and W. Melville, 2007: Surface gravity wave effects in the oceanic boundary layer: Large eddy simulation with vortex force and stochastic breakers. *J. Fluid Mech.,* **593,** 405–452.

——, ——, and ——, 2008: Catalyzing Craik-Leibovich instabilities by breaking waves. *Proc. Fifth Int. Symp. on Environmental Hydraulics,* Tempe, AZ, International Association of Hydraulic Engineering and Research, 171–184.

——, L. Romero, J. McWilliams, and W. Melville, 2012: Transient evolution of Langmuir turbulence in ocean boundary layers driven by hurricane winds and waves. *J. Phys. Oceanogr.,* **42,** 1959–1980.

Terray, E., M. Donelan, Y. Agrawal, W. Drennan, K. Kahma, A. Williams, P. Hwang, and S. Kitaigorodskii, 1996: Estimates of kinetic energy dissipation under breaking waves. *J. Phys. Oceanogr.,* **26,** 792–807.

Weller, R., and J. Price, 1988: Langmuir circulations within the oceanic mixed layer. *Deep-Sea Res.,* **35,** 711–747.

Wu, J., 1983: Sea-surface drift currents induced by wind and waves. *J. Phys. Oceanogr.,* **13,** 1441–1451.

Zikanov, O., D. Slinn, and M. Dhanak, 2003: Large eddy simulations of the wind-induced turbulent Ekman layer. *J. Fluid Mech.,* **495,** 343–368.